



UNIVERSITY OF LEEDS

This is a repository copy of *Heterostructure-based devices with enhanced humidity stability for H₂ gas sensing applications in breath tests and portable batteries*.

White Rose Research Online URL for this paper:
<https://eprints.whiterose.ac.uk/175197/>

Version: Accepted Version

Article:

Lupan, O, Ababii, N, Mishra, AK et al. (9 more authors) (2021) Heterostructure-based devices with enhanced humidity stability for H₂ gas sensing applications in breath tests and portable batteries. *Sensors and Actuators, A: Physical*, 329. 112804. ISSN 0924-4247

<https://doi.org/10.1016/j.sna.2021.112804>

© 2021, Elsevier. This manuscript version is made available under the CC-BY-NC-ND 4.0 license <http://creativecommons.org/licenses/by-nc-nd/4.0/>.

Reuse

This article is distributed under the terms of the Creative Commons Attribution-NonCommercial-NoDerivs (CC BY-NC-ND) licence. This licence only allows you to download this work and share it with others as long as you credit the authors, but you can't change the article in any way or use it commercially. More information and the full terms of the licence here: <https://creativecommons.org/licenses/>

Takedown

If you consider content in White Rose Research Online to be in breach of UK law, please notify us by emailing eprints@whiterose.ac.uk including the URL of the record and the reason for the withdrawal request.



eprints@whiterose.ac.uk
<https://eprints.whiterose.ac.uk/>

Heterostructure-Based Devices with Enhanced Humidity Stability for H₂ Gas Sensing Applications in Breath Tests and Portable Batteries

Oleg Lupan,^{a,b,*} Nicolai Ababii,^b Abhishek Kumar Mishra,^c Mani Teja Bodduluri,^d Nicolae Magariu,^b

Alexander Vahl,^e Helge Krüger,^a Bernhard Wagner,^d Franz Faupel,^e

Rainer Adelung,^{a,*} Nora H. de Leeuw,^{f,g,*} Sandra Hansen^{a,*}

^a *Institute for Materials Science, Chair for Functional Nanomaterials, Faculty of Engineering, Kiel, Kaiserstraße 2, D-24143 Kiel, Germany*

^b *Center for Nanotechnology & Nanosensors, Department of Microelectronics & Biomedical Engineering, Faculty CIM, Technical University of Moldova, 168 Stefan cel Mare str., MD-2004, Chisinau, Republic of Moldova*

^c *School of Engineering, Department of Physics, University of Petroleum and Energy Studies, Bidholi via Premnagar, 1Dehradun, 248007, India*

^d *Institute for Materials Science, Chair for Materials and Processes for Nanosystem Technologies, Christian-Albrechts-University of Kiel, Kaiser str. 2, D 24143, Kiel, Germany*

^e *Institute for Materials Science, Chair for Multicomponent Materials, Faculty of Engineering, Kiel, Kaiserstraße 2, D-24143 Kiel, Germany*

^f *School of Chemistry, University of Leeds, Leeds LS2 9JT, United Kingdom*

^g *School of Earth Sciences, Utrecht University, Princetonlaan 8a, 3584 CB Utrecht, The Netherlands*

*Corresponding authors

Prof. Dr. Lupan,	Prof. Dr. Adelung	Prof. Dr. de Leeuw	Dr. Hansen
E-mails: ollu@tf.uni-kiel.de	ra@tf.uni-kiel.de	n.h.deleeuw@leeds.ac.uk	sn@tf.uni-kiel.de
oleg.lupan@mib.utm.md			

Keywords: humidity stability, H₂ gas sensing, heterostructures, Al₂O₃/CuO

Abstract

Semiconducting metal oxide - based gas sensors exhibit outstanding sensitivity, although humidity in the analyte typically hampers precise measurements. In this work, it was shown that a 5-6 nm thin Al₂O₃ nano-layer is particularly beneficial in reducing the interference due to humidity of *p*-type conductivity copper oxide-based gas sensors. An effective approach from chemical solutions at 75 °C and thermal annealing at 600 °C was used to grow copper oxide nano-crystallite layers.

The Al₂O₃ nano-layers were subsequently deposited on top of the copper oxide by atomic layer deposition in a high-aspect-ratio regime at 75 °C. The morphological, structural, chemical, vibrational, electronical and sensor characteristics of the heterostructured nano-crystallite layers have been studied. The final nano-Al₂O₃/CuO heterostructure showed an increase in the response to H₂ gas by 140 %, while long-term stability at low and high relative humidity was observed. The initial sensing response varied by only 10% for an Al₂O₃ layer of 5-6 nm/CuO with a post-thermal annealing at 600 °C acting as an effective barrier for water vapor and oxygen. A comparison with CuO nano-crystallite layers covered with 6 nm and 15 nm of Al₂O₃ ALD ultra-thin films on top demonstrates the exceptional stability of the hydrogen gas response at high relative humidity (84 % RH). Density functional theory-based calculations show that the H₂ molecule spontaneously dissociates over the formed Al₂O₃/CuO heterostructure, interacting strongly with the surface Al atoms, showing different behavior compared to the pristine CuO (111) surface, where H₂ gas molecules are known to form water over the surface. The present study demonstrates that a thorough optimization of technology and surface properties due to coverage and formation of heterostructured nano-materials improves the humidity stability during H₂ gas sensing applications which is important for real-world applications, e.g. portable battery analysis, H₂ breath tests, along with environmental, medicine, security, and food safety diagnostic tests.

1. Introduction

A variety of semiconductor metal oxides (SMO) of different compositions are fabricated as nano-crystallite thin films for either gas sensing devices or as active layers for chemi-resistor based sensing applications. A significant amount of data has been published on the characteristics, structure and performance of sensor structures composed of different SMO materials [1–4]. However, the sensitivity of almost all conductometric sensors to water vapor [5,6] is one of the

major challenges for their practical application. The water in the analyte or tested ambience leads to a decrease or disappearance of the response, as well as fatal errors in the SMO sensors [7].

To reduce the effect of humidity and water in the analyte or tested ambience on the sensor performance, additional, co-deposited materials on the sensor surface can be employed, e.g. ultra-thin films, organometallic films [8], metal-organic compounds based on zeolitic imidazolate frameworks [9], or tin dioxide powder by spark discharge [10]. Konvalina and Haick have reported the influence of the relative humidity on micro- and nano-particle-based chemical sensors for real-world purposes and the importance of humidity compensation [11]. Garg *et al.* have reported that the long-term drift of chemi-resistor characteristics based on Au metal mono-layer-capped nanoparticles (NPs) can be decreased by capping them with tri-thiols rather than mono-thiols, thus slowing down the oxidation process of the surface thiolates [12]. Javey *et al.* have reported an approach to eliminate effects of response/sensitivity to relative humidity (RH) for chemical-sensitive field-effect transistors (FET) by employing micro-heaters [13].

The continuous monitoring of various biological and gaseous species that contain humidity in their surroundings is of high importance due to hazardous emissions, breath tests, and environmental pollution, but implementation remains challenging. For example, hydrogen gas breath tests are developed to investigate pathophysiology of gastrointestinal diseases or intestinal disorders [14]. It is well known that intestinal bacteria in the bowel yield H₂ gas on fermentation of carbohydrates, most commonly lactulose, in patients with suspicious small intestinal bacterial overgrowth [15,16]. Bacteria in the bowel can do so only if dietary carbohydrates are not absorbed in the small intestine and remain as undigested material as they transit along the digestive tract to the large intestine. Thus, glucose H₂ gas breath tests that are immune to relative humidity (RH) from the exhaled atmosphere can help significantly to overcome current challenges in diagnosis and to develop new portable devices for biomedical applications, since existing breath test structures pose several challenges due to the effect of RH on the signal. Appropriate and

convenient appraisals of diagnostic tests can reduce healthcare costs and increase the specificity of care to patient [17]. The quality of the real information received from diagnostic tests can be enhanced if the methodology and approach of the test development meets all standards related to quality [17]. In this context, the most important qualities of semiconductor metal oxide-based hydrogen gas sensors are the gas sensitivity, gas response, response and recovery times, operating temperature, temperature stability, and especially the selectivity. All these characteristics are extensively investigated and improved in the development of new materials [18–21]. For example, it is known that adsorption of H₂O molecules on oxide surfaces of SMOs will decrease the H₂ gas response [19,20,22–24]. In our previous work [5], the effect of relative humidity on the response of nanostructured films on Zn-doped copper oxide was demonstrated. Moreover, Hübner *et al.* [6] demonstrated the effect of humidity on CO detection based on thick CuO films. However, further investigation is essential to increase the stability and to reduce the interference of relative humidity and enhance reliable long-term operation, since RH significantly affects sensor performances. For example, it is important to note, that relative humidity is the main cause of the lack in performance of SMO sensors. Even at very low values of RH, most SMO sensors are strongly affected, as reported by Wicker *et al.*, where the sensor resistance was already affected at low RH of 0.1 % [25], and with increasing RH, the sensor response is affected even more [25,26]. Thus, many efforts are made worldwide to reduce the influence of RH in the test environment as a major factor to improve the quality of hydrogen sensing in breath tests, especially by semiconductor oxide-based sensors [19,20].

The surface reaction among the adsorbed oxygen species and the H₂O will reduce the baseline electrical resistance of the sensing material, thus lowering the gas response value [19,20]. Additionally, H₂O molecules adsorbed on the semiconducting oxide surface will block active surface sites, thereby lowering the gas response even further. In addition to these considerations, the RH influences the sensing performance of oxide materials in terms of sensor stability and reliability [27], since it affects repeatability of the sensing performance.

Another important aspect to consider are the “necks” between crystal grains, their sizes, and boundaries along with surface defects that can change during long-term operation at high temperatures, leading to a variation of H₂ responses under the same conditions and decreased sensor stability [19,28]. Therefore, the protection of the sensing film with an additional thin oxide layer using high aspect ratio deposition, e.g. by atomic layer deposition (ALD) of another oxide as ultra-thin layer on top, would contribute to solving this issue. In ALD, alternating pulses of chemical precursor vapors are injected onto the sample surface to form a single atomic layer each cycle. Furthermore, this method allows the accurate control of the film thickness at the nanometer scale. Consequently, a pinhole-free and uniform film is grown, which acts as a barrier to water vapor and oxygen. Moreover, the long-term stability, which is a key factor for gas sensors from polycrystalline materials, can be improved as well. Thus, the influence of humidity on the H₂ gas response should be eliminated, either through the design of the materials (surface structure and facet control) [29], by exploring different device structures, or by inducing humidity compensation to the response/sensitivity in the driving circuit, which otherwise deteriorate the practical applications of the oxide-based sensors.

In this work CuO nano-crystallite layers covered with 6 nm and 15 nm of Al₂O₃ ALD ultra-thin films are presented with exceptional stability and a hydrogen gas response at high relative humidity (84% RH). Heterostructure oxide-based H₂ gas sensors that show extraordinary selectivity over other gaseous molecules and stability in the presence of humidity are reported. The sensing characteristics of such heterostructures are drastically improved by the heterojunction formed with the top Al₂O₃ layer on CuO polycrystalline films. This enhancement is linked to the exploitation of the electronic sensitization and surface structuring, which will be discussed in detail.

2. Experimental methods

2.1 Sample synthesis

Sample synthesis from chemical solutions (SCS) followed by thermal treatment/annealing (TA) were used to prepare copper oxide nanocrystalline layers on a glass substrate [30]. The copper-complex aqueous solution, as cation bath, was made by a 0.9 M $\text{CuSO}_4 \cdot 6\text{H}_2\text{O}$ and 0.9 M $\text{Na}_2\text{S}_2\text{O}_3 \cdot 6\text{H}_2\text{O}$. Deposition cycles of copper oxide film consist of consecutive steps: (a) substrate holding in the alkali bath (81 °C) for the adsorption of the ions OH^- on the microscope specimen; (b) substrate holding in the $\text{Na}_2\text{S}_2\text{O}_3 \cdot 5\text{H}_2\text{O}$ for reaction of the Cu^+ with adsorbed OH^- .



Conventional thermal treatment in a furnace at 600 °C for 30 min was used for post-deposition thermal annealing (TA), which approach significantly improves the crystallinity of the SCS grown copper oxide layers.

Al_2O_3 ultra-thin film growth via thermal ALD was realized using Picosun's R200 with the deposition temperature during the process adjusted to 75 °C. Additionally, PicoflowTM technology was utilized to achieve conform and uniform nano-layers with high aspect ratio (HAR). Trimethylaluminum (TMA) was used as the aluminum source and H_2O to oxidize chemisorbed TMA. Alternating pulses of the aforementioned precursors were pulsed into the reactor chamber for 0.1 s per pulse to grow monolayers of Al_2O_3 . Nitrogen gas was used to transport the precursor vapors into the reaction chamber and to purge byproducts from the reactor.

2.2 Sample characterization

The morphology of the hetero-structured specimens was investigated by Carl Zeiss SEM (6 kV, 8 μA). The analysis of composition was performed by EDX, in connection with Carl Zeiss SEM. Crystallographic spectra were measured with diffractometer X-ray (XRD) using a unit Seifert3000TT, at 35 mA and 40 kV, with $\text{CuK}\alpha 1$ irradiation ($\lambda=1.540598 \text{ \AA}$). A microRaman

study was executed using a WITec Raman spectrometer, with a 532 nm Nd-YAG laser, a Peltier-cooled detector.

Additional data on the stoichiometry and chemical composition of the 6 nm Al₂O₃/CuO heterostructures were measured by XPS (OmicronNanoTechnology with Al-anode, 240 W). After collecting the spectra, potential charging of the sample was corrected by setting the C1s line of aliphatic carbon to the reference value of 284.5 eV [31]. For the evaluation, the software CasaXPS (version 2.3.16) was employed. The sensing performances to test gas were using a heterostructure detector connected to gold electrodes (see Fig. 1(e-g)). The measuring apparatus is linked to a set-up with gas flow as described in previous works [20,27,32]. The responses (R) to gases were defined according to the expression $((R_{gas} - R_{air})/R_{air}) \cdot 100$, having R_{air} and R_{gas} as the electrical resistances of the heterostructure when placed under atmosphere (R_{air}) and exposed to test gas or vapors (R_{gas}), respectively. While varying the operating temperature (OPT), volatile organic compounds (VOCs) and hydrogen were used as test gas or vapors with a flow of 500 sccm (ml/min) set using pre-calibrated mass flow controllers [32] and the required concentrations were obtained using the following equations to obtain the sensor performances of the specimen [33,34]:

$$C \text{ (ppm)} = \frac{C_1 \cdot F_{gas}}{F_{tot}} \quad (2)$$

where C is the required concentration of gas; C_1 is the initial concentration of the test gas; F_{gas} is the gas flow; and F_{tot} is the total flow of the gas-air mixture.

$$V_x = (Vol \cdot C \cdot M) / (22.4 \cdot d \cdot p) \cdot [(273 + T_r) / (273 + T_c)] \cdot 10^{-9} \quad (3)$$

where V_x is the volume of VOC injected; Vol is the test chamber volume; C is the required VOC concentration (ppm); M is the molar mass; d the density (g/cm³); p the purity; T_r the room temperature; and T_c is the test chamber temperature (operating temperature).

By measuring continuously, the output voltage across the heterostructure-based specimen, using a source meter (Keithley 2400) connected to a PC with suitable LabView (National Instruments) interface, the electrical conductivity was recorded under ambient atmosphere and exposed to test

gas or vapors (VOCs and hydrogen). During the measurements the relative humidity was set using a bubbling system and was measured using a standard hygrometer [35].

2.3 Calculation details

Electronic structure calculations were carried out within a plane wave pseudopotential implementation of the density functional theory (DFT), using the projector augmented wave (PAW) method [36,37] within the Vienna ab-initio simulation package (VASP) [38–41]. Exchange correlations were treated by the generalized gradient approximation (GGA) using PBE functionals [42]. The Hubbard model was applied to improve the localisation of the Cu 3d electrons, through the formulation of Dudarev et. al. [43], where an effective correction of $U_{eff} = 7$ eV ($U_{eff} = U - J$, i.e. the difference between the Coulomb U and exchange J parameters) was used to accurately describe the strong correlations in CuO. This value of the U parameter effectively reproduces the correct structural, magnetic and electronic properties of tenorite (CuO crystal) [44,45]. Other details of the calculations are the same as in previous work [44].

The (111) surface is the most stable surface of tenorite and was modelled using $3 \times 3 \times 1$ Monkhorst–Pack grid points (atomic structures were relaxed using the tetrahedron method) [46]. The locations of the atoms in the cell were fully relaxed until the atomic forces on each ion were less than 0.01 eV/Å. The electronic densities of states were computed using a dense $5 \times 5 \times 1$ Monkhorst-Pack grid point matrix, whereas a truncation kinetic energy of 450 eV for the plane waves provides an accurate description of properties that are affected by sharp features in the density of states. We used our previous slab model of four atomic layers, where the bottom two layers of atoms were fixed at their relaxed bulk positions to simulate the bulk phase of the crystal, while the atoms in the top two layers of the surface were permitted to change their atomic coordinates freely during geometry optimization [44]. A vacuum region of more than 15 Å was

used between surface slabs to avoid interactions between the periodic images while modelling the molecule-surface interactions.

For the investigations of the interactions of the gas molecules with the surface, we have incorporated long-range dispersion forces using the DFT-D2 approach by Grimme [47]. The adsorption energies of the gas molecule were calculated using the relation:

$$E_{ads} = E_{complex} - (E_{surface} + E_{molecule}), \quad (4)$$

where $E_{complex}$ is the total energy of the surface slab with adsorbed molecule, $E_{surface}$ is the energy of the surface slab without molecule, and $E_{molecule}$ is the energy of the isolated molecule. $E_{molecule}$ was calculated by modelling the isolated molecule in the centre of a broken symmetry cell with lattice constants of 20 Å, sampling only the gamma-point of the Brillouin zone with the same set of parameters as described for the surfaces. Bader charge analyses were performed using the code developed by Henkelman and co-workers [48,49] to investigate the charge transfer between the surface and molecule.

3. Results and discussions

3.1 Morphological Investigations of Al₂O₃/CuO

Morphology and SEM images of Al₂O₃/CuO heterostructures with a 6 nm top layer of Al₂O₃ after thermal treatment at 600 °C for 30 min are shown in **Fig. 1(a-d)**. The investigated samples are formed of densely packed CuO grains that homogeneously cover the specimen. Agglomerates or gaps were not found, even at lower magnification (see **Fig. S1**). The diameter of the crystalline CuO grains fluctuates in a diapason from 100 nm to 450 nm (**Fig. 1(b,c)** and **Fig. S2**). At higher magnification (see **Fig. 1(b,c)** and **Fig. S2(b,c)**), a nanodot-like structure is observed for 6 nm-Al₂O₃/CuO heterostructures after TA at 600 °C for **30 min** in comparison with as-grown samples with 6 nm-Al₂O₃/CuO (see **Fig. S2(a)**). These nanodot-like structures appear only for samples

after thermal annealing at about 600 °C for 30 min, probably due to phase transitions at the interface or surface of the 6 nm-Al₂O₃/CuO. This process leads to the formation of nano-agglomerations of CuAl₂O₄ (see Fig. 1(g)), following the energy stress that occurs in this specific thermal annealing temperature range [50–52].

3.2 XRD, Raman and XPS studies

X-ray diffraction was selected to obtain the crystal structure of the Al₂O₃/CuO heterostructures after TA at 600 °C for 30 min. Fig. 2(a) shows that, for 6 nm-Al₂O₃/CuO heterostructures after TA at 600 °C for 30 min, the two phases of CuO and CuAl₂O₄ can be identified. As reported in our previous work [30], at temperatures above 550 °C, only monoclinic CuO is present with highest XRD reflections detected for (-111)/(002) and (111) at 2 θ angles of 35.45° and 38.7°, respectively. The shape of the diffraction peaks indicates the high crystallinity of the investigated samples. The tenorite structure has space group *C2/c* [53] with crystal lattice parameters of $c = 5.1321 \text{ \AA}$, $a = 4.6851 \text{ \AA}$, $b = 3.4231 \text{ \AA}$, and $\beta = 99.52^\circ$ [54]. The copper in tenorite is in the Cu²⁺ oxidation state showing antiferromagnetic ordering [54] and antiferromagnetic insulating ground states [55,56]. For 15 nm-Al₂O₃/CuO heterostructures after TA at 620 °C for 40 min the two phases of CuO and CuAl₂O₄ were also identified (see Fig. S3).

The crystalline phase of CuAl₂O₄ was identified from Card PDF #01-1153 (copper aluminum oxide) to be a cubic system with the precise lattice parameter of $a = 8.064 \text{ \AA}$ [50,57].

In Fig. 2(b), the Raman spectrum of 6 nm-Al₂O₃/CuO heterostructures at room temperature of 20 °C enclosed by 70 and 1000 cm⁻¹ is shown. From the spectrum, the mode peaks observed at about (i) 281, 326 and 617 cm⁻¹, assigned to the tenorite [5,30], and (ii) 481, 512, 608, 703 and 788 cm⁻¹, which are assigned to the CuAl₂O₄ (copper aluminium oxide), confirm the existence of the two phases, also indicated by XRD [50]. Raman mapping image of the A_g mode (281 cm⁻¹) for

the 6 nm Al₂O₃/CuO heterostructures and TA at 600 °C in air for 30 min is shown in **Fig. S4**. The CuO structure has 12 phonon branches due to its primitive cell, so the modes are [5,55]:

$$\Gamma_{vibr} = A_g + 2B_g + 4A_u + 5B_u \quad (5)$$

where $A_u + 2B_u$ are three acoustic modes; $A_g + 2B_g$ are nine Raman-active optical modes; and $3A_u + 3B_u$ are six IR-active modes [5,58]. The IR modes implicate the motion of Cu and O atoms and the induced dipole moment is onward of axis b for A_u modes and vertical to axis b for the B_u modes [5]. In the B_g and A_g Raman modes, the O atoms move perpendicular to the b -axis for B_g modes and in the b -direction for A_g [5,58].

The structure of CuAl₂O₄ is an inverse cubic spinel with space group O_h-Fd3m . The lattice vibrations which are active optically in different symmetry species are [50,59]:

$$\Gamma = A_{1g} + E_g + 3F_{2g} + 5F_{1u} + F_{1g} + 2A_{2u} + 2E_u + 2F_{2u} \quad (6)$$

where A_{1g} , $3F_{2g}$ and E_g are Raman-active modes; and F_{1u} are infrared-active modes. In the $5F_{1u}$ modes, one mode with zero frequency corresponds to a translation mode, but the other four modes are detected in the infra-red region. There is a single micro-Raman mode which is inactive, F_{1g} , while $2E_u$, $2A_{2u}$ and $2F_{2u}$ are inactive infrared modes. The band at ~ 788 cm⁻¹ has been attributed to A_{1g} , showing the vibrations of M_t-O₄ tetrahedra (M_t, tetrahedral cation), bands at ~ 608 , 512 and 703 cm⁻¹ have been attributed to the F_{2g} mode, due to Cu-O vibrations, and the sluggish mode at 481 cm⁻¹ has been assigned to the E_g mode, conforming to the curving mode of Al-O tetrahedral [50,51,59,60].

The XPS investigation of 6 nm-Al₂O₃/CuO heterostructures indicates the presence of Na, O, Cu, C and Al, which can be identified in the XPS survey spectrum, shown in **Fig. 2(c)**. The signal corresponding to C stems from surface contaminations by atmospheric carbon and occurs as a result of the ALD layer, where TMA organic material, i.e. Al(CH₃)₃, was used as the aluminum precursor. The signal corresponding to Na, Cu and Al is attributed to the Al₂O₃/CuO

heterostructures. The signal of O is partially related to atmospheric contaminations but mainly to oxidation of Na, Cu and Al from the sample. The occurrence of a Na signal can be assigned to the uncovered surfaces or the migration/transfer of sodium ions from the substrate made of microscope glass to the 6 nm- $\text{Al}_2\text{O}_3/\text{CuO}$ heterostructures [61–63].

A closer look at the high-resolution spectrum of the Al-2p lines, shown in **Fig. 2(d)**, reveals that the main peak of the Al-2p line is located around 73.9 eV. Due to the limitations of the measurement set-up, it is not possible to resolve the peak splitting between Al-2p_{3/2} and Al-2p_{1/2}. The peak location around 73.9 eV agrees well with Al³⁺ in Al_2O_3 , which is commonly reported between 73.7 eV and 74.8 eV [31,64]. The occurrence of an additional shoulder, ranging from the main peak towards higher binding energies is on the one hand due to an overlap with the Cu-3p lines (typically located around 76 eV) [31] and on the other hand potentially due to the presence of a different chemical environment, e.g. in Al_2CuO_4 (typically reported between 74.2 eV and 74.7 eV) or the Al-OH bonds in for example $\text{Al}(\text{OH})_3$ (typically reported between 74.0 eV and 75.7 eV) [31,64].

As observed in the high resolution spectrum of the Cu-2p lines in **Fig. 2(d)**, the peak position of the Cu2p_{3/2} line is centred at ~934.8 eV, which is an indication of the presence of Cu²⁺ in CuO (typically located between 933.2 eV and 934.4 eV) rather than Cu⁺ in Cu₂O (commonly reported between 932.0 eV and 932.7 eV) or metallic Cu (between 932.2 eV and 933.0 eV) [31,64–66]. Also, the occurrence of satellite peaks to the Cu-2p_{3/2} line around 942.6 eV and 944.9 eV supports the assignment to Cu²⁺ in CuO.

However, based on the high sensitivity of the surface for XPS, the presence of Cu and Al in different oxidation states within the bulk of the 5 nm- $\text{Al}_2\text{O}_3/\text{CuO}$ may not be ruled out here.

3.3 Gas sensing properties

Fig. 3(a) presents the response to various gases (hydrogen, *n*-butanol, ethanol, 2-propanol, acetone, carbon dioxide, methane and ammonia) with concentrations of 100 ppm by the 6 nm-

Al₂O₃/CuO heterostructures at different working temperatures. The gas response shows *p*-type conductivity behaviour for all tested gases, since the electrical resistance increased after the introduction of the gases. Furthermore, a high and selective response to H₂ at all working temperatures was observed. The responses are ~50%, ~86%, ~140%, ~131% and ~109% at working temperatures of 250 °C, 275 °C, 300 °C, 325 °C and 350 °C, respectively, and the optimal operating temperature was 300 °C. For comparison, **Fig. S5(a)** shows the data for CuO nanostructures without an additional Al₂O₃ top layer (TA 600 °C for 30 min) with response/selectivity to ethanol vapors at OPT of 250 °C and to H₂ gas at higher working temperatures. **Fig. 3(b)** illustrates the characteristic current-voltage curves of 6 nm-Al₂O₃/CuO heterostructures after TA at 600 °C for 30 min at various working temperatures, i.e. an increase of the electrical current with operating temperature and proven Ohmic behavior with a linear characteristic. **Fig. 3(c)** shows the dynamic hydrogen response of 6 nm-Al₂O₃/CuO heterostructures with TA at 600 °C at various working temperatures. Response and recovery times are $\tau_r = 14.5$ s, 21.2 s, 18.7 s, 22.7 s and 22.8 s and $t_d = 56.1$ s, 48.1 s, 56.3 s, 55.8 s, 47.1 s at working temperatures of 250 °C, 275 °C, 300 °C, 325 °C and 350 °C, respectively. **Fig. 3(d)** presents the dynamic response to different concentrations of hydrogen (1, 5, 10, 50, 100, 500 and 1000 ppm) at a working temperature of 300 °C for the 6 nm-Al₂O₃/CuO heterostructures after thermal annealing at 600 °C for 30 min under low relative humidity (16 % RH, curve 1) and high relative humidity (84 % RH curve 2). For example, a response of ~27 % is measured at 1 ppm H₂. Here, the differences in response for low and high relative humidities for 1, 5, 10, 50, 100, 500 and 1000 ppm H₂ can also be observed, indicating changes of ~10%, ~11%, ~13%, ~17%, ~16%, ~7% and ~28%, respectively, from the maximum response for each concentration. For a better understanding of the effect of working temperature and relative humidity on the sensors, they are plotted in **Fig. S6(a,b)** using the real values of the sensor resistance. Comparing the data obtained for 6 nm-Al₂O₃/CuO heterostructures with the CuO nanostructures in **Fig. 4(c)**, the high RH leads to a reduction in the H₂ response by on average 35-40% for CuO. Furthermore, the response to

ethanol vapor (**Fig. S5(b)**) is drastically decreased at high RH, resulting in an approximately zero response. In contrast, the 6 nm-Al₂O₃/CuO heterostructures demonstrate excellent response at the high relative humidity.

The error bars express the maximum and minimum values of the response measured from four tested sensor sets of each heterostructure at given concentrations of vapors exposed to 16% and 84% RH (see **Fig. 3(f)**). **Fig. 3(e)** exhibits the dynamic gas response to 5 ppm of hydrogen for 6 nm-Al₂O₃/CuO heterostructures at an OPT of 300 °C. Here, the effect of the relative humidity on the sensing of low concentrations of hydrogen gas is negligible. **Fig. 3(f)** displays the gas response versus concentration of hydrogen gas from 1 ppm to 1000 ppm at an OPT of 300 °C. At lower concentrations of test gases, the response is high and increases with higher concentration; in addition, at high relative humidity an increased stability is observable. This might be explained by the high aspect ratio and conformal coverage of the deposited nano-layer (5-6 nm) of Al₂O₃ on *p*-type CuO grains compared to the unprotected structure, which does not affect the surface-area-to-volume-ratio, but the surface chemistry.

The dynamic response to multiple types of vapors at a working temperature of 300 °C of the 6 nm-Al₂O₃/CuO heterostructures is displayed in **Fig. S7(a)**, indicating high selectivity to hydrogen gas. The dynamic response with three consecutive pulses to hydrogen with 100 ppm gas concentration at a working temperature of 300 °C of 6 nm-Al₂O₃/CuO heterostructures after thermal treatment at 600 °C during 30 min is presented in **Fig. S7(b)**. Here, the superior sensing performances, with excellent repeatability, make this system highly useful for practical applications and for the development of real devices.

Figures 4(a,b) show the long-term stability of 6 nm-Al₂O₃/CuO heterostructures under low (16%) and high (84%) relative humidity and the response over 70 days to H₂ gas at a working temperature of 300 °C with concentrations of 1 ppm (**Fig. 4(a)**) and 100 ppm (**Fig. 4(b)**). We note, that after 70 days the gas response is approximately constant, varying by only 10-15%,

demonstrating the long-term stability of the sensors. The long-term stability toward H₂ gas with concentrations of 5 ppm from **Fig. S8** shows approximately the same stability within 10%. **Fig. 4(c)** shows the response to H₂ gas versus various working temperatures for low and high relative humidity of CuO nanostructures after thermal annealing at 600 °C for 30 min. Here, the high RH leads to a reduction in the H₂ response by 35-40 %.

Fig. 5(a) shows the gas response to various gases (hydrogen, *n*-butanol, 2-propanol, ethanol, acetone and ammonia) with a concentration of 100 ppm for 15 nm Al₂O₃/CuO heterostructures after thermal annealing at 620 °C for 40 min. **Fig. 5(a)** shows that, independent of the working temperatures (275 °C, 300 °C, 325 °C and 350 °C), the sample is selective to hydrogen gas with response values of ~51 %, ~54 %, ~61 % and ~75 %, respectively. **Fig. 5(b)** shows the current-voltage characteristic of 15 nm Al₂O₃/CuO heterostructures after TA 620 °C during 40 min at different operating temperatures. The samples show Ohmic behavior with a linear characteristic and the current decreases with the operating temperature compared to the 6 nm Al₂O₃/CuO sample (**Fig. 3(b)**), possibly due to the thicker layer (15 nm) of Al₂O₃. **Fig. 5(c)** shows the dynamic response to hydrogen of 15 nm Al₂O₃/CuO heterostructures after TA at 620 °C for 40 min at different operating temperatures, with values of $\tau_r = 17.4$ s, 18.3 s, 19.7 s, 20.8 s and $t_d = 61.3$ s, 63.2 s, 60.1 s, 59.9 s for the response and recovery times at working temperatures of 275 °C, 300 °C, 325 °C and 350 °C, respectively.

Fig. 5(d) presents the dynamic response to multiple concentrations of hydrogen (1, 5, 10, 50, 100, 500 and 1000 ppm) at a working temperature of 350 °C of 15 nm Al₂O₃/CuO heterostructures after thermal annealing at 620 °C for 40 min for low RH (curve 1) and high RH (curve 2). It can be observed that the high RH does not affect the sensor even at low hydrogen concentrations (1 ppm), where a 9% response was obtained (see **Fig. 5(e)**). Whereas for the 6 nm Al₂O₃/CuO sample (**Fig. 3(d)**) at high relative humidity the response is still affected by 10-15%, the 15 nm Al₂O₃/CuO sample shows no change in the response. **Fig. 5(f)** shows the gas response versus concentration of hydrogen gas from 1 ppm to 1000 ppm at an OPT of 350 °C. At relatively low concentrations, the

response is high and increases with higher concentrations. In addition, at high relative humidity the increased stability is observable, which might be explained by the high aspect ratio conformal coverage of the deposited thicker nano-layer (15 nm) of Al₂O₃ on *p*-type CuO grains.

The gas detection studies of nano-Al₂O₃/CuO heterostructures, showing the high selectivity for H₂ gas, the stability in long-term usage, stability under humidity, as well as the detection of very low concentrations of only 1 ppm, suggest that an important application field could be the monitoring of thermal runaway in Li-ion-batteries (LIBs). LIBs with a critical failure (short circuit, damage, etc.) can trigger a chain of exothermic reactions that leads to a rapid rise in temperature and consequent catastrophic self-accelerated degradation (thermal runaway) of the LIB, with the elimination of hydrogen and hydrocarbons [67]. Moreover, hydrogen is one of the most common gases found in LIB after long-term cycling and/or storage at elevated/high temperatures [68]. H₂ gas production in LIBs is assigned to residual moisture, due to insufficient drying of the electrodes, separators and other cell components. Even small amounts of H₂O contamination inside the electrolyte can lead to multiple electrolyte degradation and corrosion reactions at the electrode/electrolyte interfaces [68–70]. Applying nano-Al₂O₃/CuO heterostructure sensors close to individual battery cells could identify units that are failing from the H₂ gas eliminated, thus indicating probable thermal runaway that can heat LIBs to over 200 °C by ensuring the appropriate working temperature for the sensor.

The selective detection of hydrogen, moisture stability and detection of low hydrogen concentrations by sensors based on nano-Al₂O₃/CuO heterostructures, makes their integration in the vicinity of the individual battery cells an attractive prospect, i.e. over the connecting busbars of battery cells [71], or above the battery cell [72]. Thus, a possible route to an efficient and rapid sensing of the very early phase of thermal runaway could be achieved, thereby avoiding the degradation of other parallel connected cell units.

3.4 Proposed gas detection mechanism

The mechanism for gas detection of heterostructure-based nanomaterials is still under debate. The main gas and vapor sensing models for *p*-type conductometric devices are explained as molecular adsorption, followed by a charge transfer directly between the gaseous molecules and heterostructure-based nanomaterials to produce modulation of the Fermi level, i.e. variation in the electrical conductivity. The basic gas sensing-detection mechanism of our heterojunctions can be discussed following the existing models of ionosorption [73–78].

(Co, Ni, Cu, Zn) aluminate is known as a catalytic material with a low acidity for surfaces, but high thermal and chemical stabilities for growth, hydrogenation, dehydrogenation, dehydration, isomerization and combustion processes [79–82]. As such, the response enhancement for H₂ could be interpreted as depending on the free electron and hole transfer and the charge separation owing to the CuAl₂O₄/CuO nano-heterostructure. The creation of *n-p* and *n-n* nano-heterojunctions is known to be highly valuable in improving detection characteristics [2,73–77,83].

Fig. 6 presents a schematic of the H₂ detection suggested for a CuAl₂O₄/CuO structure. A flow of electrons will leak from CuAl₂O₄ nanodots to the CuO nanostructure that is formed following the thermal annealing of Al₂O₃ at a temperature of 600 °C (see **Fig. 1(a-d)**), thereby producing an increase in the hole concentration in the CuAl₂O₄ surrounding nanodots. This situation will lead to a higher coverage of oxygen species on the CuAl₂O₄ nano-island-dot surfaces in air (**Fig. 6(a)**), provoking higher hole concentrations in that region, thus improving reactions on the surface, e.g. the absorption of a test gas if the heterostructure was exposed to gas. Upon application of hydrogen gas (**Fig. 6(b)**), adsorption and reaction with oxygen will take place, enhancing the response, based on a smaller charge transfer value on the top surface [2,73,80,84].

The detection steps suggested here illustrate that the existence of CuAl₂O₄ will enhance the adsorption of species on the CuAl₂O₄ surface, because transfer of free charge carriers from CuO to CuAl₂O₄ will speed up the oxidation processes. The improvement of surface reactions such as

adsorption, dissociation, and the ionization of oxygen through the presence of different nanoparticles of metal oxides, for example NiO and In₂O₃, has been recognized previously [85,86].

At operating temperatures of 250 – 350 °C in ambient air (the ranges of temperature involved for current investigation), the adsorbed species on the surface of metal oxides is principally molecular oxygen (O₂), which takes a free hole in a top surface state, (see **Fig. 6(a)**) according to the equation [73,78,80,87]:



For hetero-structures, this process will contribute to the appearance of a depletion region at the top of the surface.

Next, upon exposure to hydrogen gas the following reaction takes place [21,83,88,89]:



Two H₂O molecules are formed and the holes in the depleted region will recombine with the released electrons forming Null ($h^+ + e^- \rightarrow Null$). Next occurs a narrowing of the depletion region and a decrease in the electrical current or an increase in the resistance of the heterostructure.

3.5 Breath test sensing

Fig. 7(a) illustrates schematically the principle of a hydrogen and/or methane breath test. Initially, bacterial fermentation of a badly absorbed sugar takes place in the intestines, where hydrogen and/or methane gas is produced. Thus, hydrogen and/or methane gas is absorbed into the bloodstream and transported to the lungs (see **Fig. 7(a)**, step 1). Upon these gases from the blood flow reaching the lungs, they are transported by exhalation (see **Fig. 7(a)**, step 2). The breath can be analyzed, representing a very useful non-invasive investigation method. **In our case, the breath tests were performed as follows: at the working temperature of 300 °C, first a flow of H₂ gas with a concentration of 75 ppm was applied to the sample; at the same time as the H₂ gas, an**

expiration of air from a person was applied for 10 seconds to obtain the second pulse in **Fig. 7(b)**; whereas the third pulse in this figure is obtained solely from the expiration of air from a person to see the influence of the response on breath dependence. **Fig. 7(b)** shows the effect of breath on the hydrogen response. It can be seen that the first pulse, where only hydrogen gas is applied with a concentration of 75 ppm at a working temperature of 300 °C, leads to a response of 112%. A second pulse, applied for 10 seconds and composed of 75 ppm of hydrogen gas and a test-breath, leads to a maximum response of 121%. Here, the test-breath showed no effect on the response, which proves the excellent stability of the sensor. Only in the third pulse, upon application of the test-breath only, a negligible response of about 5% is shown, explaining the high response to the second pulse of 121%. For comparison, **Fig. S9** shows the effect of breath on the hydrogen response under longer exposure of 25 seconds, when 75 ppm of hydrogen gas is applied in the second pulse. This also had low impact on the sensing performance.

3.6 DFT calculations: H_2 molecule interaction with Al_2O_3 -CuO (111) surface

The (111) surface was found to be the dominant plane in the CuO morphology, with the lowest surface energy of 0.75 J/m² [44]. The atomic top layer of the CuO (111) surface contains two 3- and two 4-coordinated copper and oxygen atoms. 3-coordinated Cu_{CUS} are coordinatively unsaturated atoms, and 4-coordinated Cu_{CSA} are coordinatively saturated copper atoms, both present in the top layer (see **Fig. S10**). O_{SUF} are the most exposed 3-coordinated oxygen atoms, whereas O_{SUB} are 4-coordinated sub-surface oxygen atoms. We first relaxed the surface with the optimized geometry shown in **Fig. S10**. In order to model the Al_2O_3 :CuO (111) surface, we replaced 3 Cu atoms with 2 Al atoms to maintain charge neutrality and we considered both the top surface layer as well as the second Cu-O layer. Different configurations were investigated by substitution of various copper atoms in the first and second layers and we found the lowest energy structure to be one, where we had removed one 4-coordinated copper (Cu_{CSA}) atom from the top layer and substituted one 4-coordinated (Cu_{CSA}) and one 3-coordinated (Cu_{CUS}) atom with Al atoms. After relaxation, we noted that one of the aluminium atoms, Al1, which was substituted for

the 4-coordinated copper atom Cu_{CSA} , binds to three oxygen atoms in the top surface layer, whereas the second Al atom, Al2, which was substituted for a 3-coordinated copper atom Cu_{CUS} , forms four Al-O bonds in the topmost surface layer, as shown in **Fig. 8**. As such, we observed formation of an Al_2O_3 -CuO heterostructure in the top layer of the surface, with Al-O bond lengths ranging from 1.711 Å to 1.884 Å.

We next placed a H_2 molecule in various orientations close to different surface sites and noted that upon geometry optimisation the molecule dissociates spontaneously, with one H atom binding to one of the surface oxygen atoms that is bonded to a surface Al atom and a second layer Cu atom, with the other H atom binding to another surface O atom that was shared between the second Al atom and a Cu_{CUS} atom in the top layer, as shown in **Fig. 9**. On adsorption, the surface Al-O and Cu-O bond lengths increase, with the Al1-O4 bond elongating from 1.73 Å to 1.80 Å, the Al2-O5 bond length increasing from 1.71 Å to 1.80 Å and Cu_{CUS} -O5 increasing to 1.94 Å from its original value of 1.81 Å.

In order to further assess the interaction of the hydrogen molecule with the Al_2O_3 -CuO (111) surface, we performed a Bader charge analysis and plotted the charge density difference, as shown in **Fig. 9(b)**. We note that as a result of the interaction with surface Al and Cu atoms, both hydrogen atoms lose charge density to gain positive charges of 0.68 and 0.70 e^- respectively, whereas the Bader charges of Al1, Al2 and the surface Cu atom, which bind the hydrogen atoms, change from 2.37, 2.41 and 1.09 e^- to 2.36, 2.43 and 0.526 e^- , respectively. In order to further quantify the electronic structure changes, we have also calculated the electronic density of states (DOS) and the results show that there is considerable shift in the conduction band, as the band gap changes from 0.88 eV to 1.09 eV (see **Fig. 10**).

The change in electronic states is also reflected in the Fermi energy, which changes from -1.808 to -1.147 eV as a result of the interaction of the hydrogen gas with the Al_2O_3 :CuO surface. The binding energy for the dissociated H_2 molecule is calculated to be -2.83 eV.

The dissociative adsorption of the H₂ molecule on the Al₂O₃:CuO surface is in contrast to the behavior on the pristine CuO (111) top surface, where we have established that the H₂ molecule forms an adsorbed water molecule through binding to the most exposed O atoms at the CuO (111) surface, thereby reducing the CuO (111) surface [90]. We have also investigated the interaction of the hydrogen molecule with the tenorite (111) top surface with a lower level of Al doping, where we used a 2x2 surface simulation cell of CuO (111), consisting of 64 Cu and 64 O atoms, and replaced 3 top layer Cu atoms by 2 Al atoms. Similar to the 1x1 cell, we selected the configuration with the lowest energy, i.e. where we had replaced two 4-coordinated copper (*Cu_{CSA}*) atoms and one 3-coordinated (*Cu_{CUS}*) atom by Al atoms. We next placed a H₂ molecule onto the surface, but observed similar dissociative adsorption of the H₂ molecule, as presented in **Fig. S11**.

To investigate the role of water on the Al₂O₃-CuO (111) surface, we next studied the interaction of an H₂O molecule, again by placing the molecule in different orientations close to Al-Cu heterostructure formed as a result of Al doping of the CuO (111) surface. We noted that the H₂O molecule dissociates into H and OH species which bind to the surface (see **Fig. 11**). The OH species binds to one of the aluminum atoms, Al1, with a bond length of 1.768 Å, while the H atom binds to one of the surface oxygen atoms, shared between the second Al atom (Al2) and a copper *Cu_{CUS}* atom. Again, this behaviour is in contrast to the interaction of a water molecule with the pristine CuO (111) surface, where no such dissociation is observed and the molecule binds instead to an unsaturated copper atom, *Cu_{CUS}* ($d_{Cu-O} = 2.08$ Å), as show in **Fig. S12**.

4. Conclusions

In this work, we have reported the synthesis of nano-Al₂O₃/CuO heterostructures with low sensitivity to humidity and an increased ratio in H₂/humidity interference/sensitivity. The proposed method allows the elimination of the effects of humidity in the response to gases by conductometric chemical-sensitive heterostructures, via the use of an ultra-thin

oxide layer formed on top of the surface through high-aspect ratio ALD. A 6 nm Al_2O_3 nano-layer was grown on top of the surface of CuO nanostructures thus obtaining a nano- $\text{Al}_2\text{O}_3/\text{CuO}$ heterostructure, which resulted in the formation of a heterojunction of CuAl_2O_4 and CuO after treatment at 600 °C for 30 min, as shown by XRD and Raman measurements. The sensor system demonstrated a high selectivity to H_2 gas with a value of ~140%, at operating temperatures of about 300 °C. Furthermore, the ability to detect small concentrations of hydrogen gas was demonstrated, obtaining a response of ~27% to a concentration of only 1 ppm, as well as a stabilizing effect at high concentrations of relative humidity. The response at 84% RH was modified by only ~10% from the response value at 16% RH, which can be explained on the basis of higher aspect ratio coverage of *p*-type CuO compared to the unprotected material. ~~The present study demonstrates that heterostructured nano-materials have enhanced humidity stability for H_2 gas sensing applications, possibly due to the low surface acidity catalytic properties, and high thermal and chemical stability of copper aluminum oxide for processes that take place on the heterostructured nano-material surface.~~

The DFT calculations have revealed the fundamentally different behaviour between the $\text{Al}_2\text{O}_3:\text{CuO}$ heretostructure and the pristine CuO (111) surface. The H_2 molecule interacts strongly with the $\text{Al}_2\text{O}_3:\text{CuO}$ (111) surfaces by dissociating into atomic hydrogens and binding to Al-bound surface oxygen atoms, in contrast with the behaviour of H_2 molecules on the pristine CuO (111) surfaces, where an adsorbed water molecule is known to form surface-bound water, due to the H_2 molecule interacting with surface oxygen atoms. Furthermore, owing to the more reactive nature of the Al-CuO heterostructure, the spontaneous dissociation of water molecules is also observed over the $\text{Al}_2\text{O}_3:\text{CuO}$ surface, again in contrast to the pure CuO (111) surface where water adsorbs molecularly.

A study into the effect of thermal annealing temperatures and durations, with respect to RH and H_2 concentrations as well as temperature, is in progress and will be published elsewhere. Our

advances in such a competitive field could contribute to the development of a cost-effective, low-power heterostructure for widespread detection of H₂ in portable battery applications, not only for gas analysis, but also for security, environmental, breath test and food safety applications.

Acknowledgment

Federal Ministry of Education and Research by the project “PorSSi” (03XP0126 B) and the EKSH for supporting this research by “3D strukturierte Kohlenstoff-Schwefel Gerüstmaterialien als neuartiges und nachhaltiges Kathodenmaterial für Hochenergie Lithium-Ionen Akkus”. Additionally, the authors thank the WTSH and the EUSH for partially funding this project BAEW with (LPW-E/1.1.2/1486). This research was funded in parts by the DFG-Deutsche Forschungsgemeinschaft (German Research Foundation) under the schemes FOR 2093, AD 183/17-1 at Kiel University and SFB 986-TP-B1 and SCHU 926/25-1 at TUHH. Dr. Oleg Lupan acknowledges the Alexander von Humboldt Foundation for the research fellowship for experienced researchers (3-3MOL/1148833 STP) at the Institute for Materials Science, Kiel University, Germany. Dr. A.K. Mishra acknowledges University of Petroleum and Energy Studies, Dehradun. Via N.H. de Leeuw’s membership of the UK's HPC Materials Chemistry Consortium, which is funded by EPSRC (EP/L000202, EP/R029431), this work used the ARCHER UK National Supercomputing Service (<http://www.archer.ac.uk>). This research was sponsored in part by the NATO Science for Peace and Security Programme (SPS) under grant G5634 „Advanced Electro-Optical Chemical Sensors” AMOXES.

References

- [1] D. Zappa, V. Galstyan, N. Kaur, H.M.M. Munasinghe Arachchige, O. Sisman, E. Comini, “Metal oxide -based heterostructures for gas sensors” - A review, *Anal. Chim. Acta.* 1039 (2018) 1–23. doi:10.1016/j.aca.2018.09.020.
- [2] D.R. Miller, S.A. Akbar, P.A. Morris, Nanoscale metal oxide-based heterojunctions for gas sensing: A review, *Sensors Actuators B Chem.* 204 (2014) 250–272. doi:10.1016/j.snb.2014.07.074.

- [3] E. Kanazawa, G. Sakai, K. Shimano, Y. Kanmura, Y. Teraoka, N. Miura, N. Yamazoe, Metal oxide semiconductor N₂O sensor for medical use, *Sensors Actuators B Chem.* 77 (2001) 72–77. doi:10.1016/S0925-4005(01)00675-X.
- [4] G. Korotcenkov, Metal oxides for solid-state gas sensors: What determines our choice?, *Mater. Sci. Eng. B.* 139 (2007) 1–23. doi:10.1016/j.mseb.2007.01.044.
- [5] V. Cretu, V. Postica, A.K. Mishra, M. Hoppe, I. Tiginyanu, Y.K. Mishra, L. Chow, N.H. de Leeuw, R. Adelung, O. Lupan, Synthesis, characterization and DFT studies of zinc-doped copper oxide nanocrystals for gas sensing applications, *J. Mater. Chem. A.* 4 (2016) 6527–6539. doi:10.1039/C6TA01355D.
- [6] M. Hübner, C.E. Simion, A. Tomescu-Stănoiu, S. Pokhrel, N. Bârsan, U. Weimar, Influence of humidity on CO sensing with p-type CuO thick film gas sensors, *Sensors Actuators B Chem.* 153 (2011) 347–353. doi:10.1016/j.snb.2010.10.046.
- [7] A.R. Hopkins, N.S. Lewis, Detection and Classification Characteristics of Arrays of Carbon Black/Organic Polymer Composite Chemiresistive Vapor Detectors for the Nerve Agent Simulants Dimethylmethylphosphonate and Diisopropylmethylphosphonate, *Anal. Chem.* 73 (2001) 884–892. doi:10.1021/ac0008439.
- [8] D.S. Vlachos, P.D. Skafidas, J.N. Avaritsiotis, The effect of humidity on tin-oxide thick-film gas sensors in the presence of reducing and combustible gases, *Sensors Actuators B Chem.* 25 (1995) 491–494. doi:10.1016/0925-4005(95)85105-4.
- [9] S.S. Nair, N. Illyaskutty, B. Tam, A.O. Yazaydin, K. Emmerich, A. Steudel, T. Hashem, L. Schöttner, C. Wöll, H. Kohler, H. Gliemann, ZnO@ZIF-8: Gas sensitive core-shell hetero-structures show reduced cross-sensitivity to humidity, *Sensors Actuators B Chem.* 304 (2020) 127184. doi:10.1016/j.snb.2019.127184.
- [10] Y. Seekaew, W. Pon-On, C. Wongchoosuk, Ultrahigh Selective Room-Temperature Ammonia Gas Sensor Based on Tin–Titanium Dioxide/reduced Graphene/Carbon Nanotube Nanocomposites by the Solvothermal Method, *ACS Omega.* 4 (2019) 16916–16924. doi:10.1021/acsomega.9b02185.
- [11] G. Konvalina, H. Haick, Effect of Humidity on Nanoparticle-Based Chemiresistors: A Comparison between Synthetic and Real-World Samples, *ACS Appl. Mater. Interfaces.* 4 (2012) 317–325. doi:10.1021/am2013695.
- [12] N. Garg, A. Mohanty, N. Lazarus, L. Schultz, T.R. Rozzi, S. Santhanam, L. Weiss, J.L. Snyder, G.K. Fedder, R. Jin, Robust gold nanoparticles stabilized by trithiol for application in chemiresistive sensors, *Nanotechnology.* 21 (2010) 405501. doi:10.1088/0957-4484/21/40/405501.
- [13] N. Gupta, H.M. Fahad, M. Amani, X. Song, M. Scott, A. Javey, Elimination of Response to Relative Humidity Changes in Chemical-Sensitive Field-Effect Transistors, *ACS Sensors.* 4 (2019) 1857–1863. doi:10.1021/acssensors.9b00637.
- [14] S.V. Rana, A. Malik, Hydrogen Breath Tests in Gastrointestinal Diseases, *Indian J. Clin. Biochem.* 29 (2014) 398–405. doi:10.1007/s12291-014-0426-4.
- [15] B. Haderstorfer, D. Psycholgin, W.E. Whitehead, M.M. Schuster, Intestinal Gas Production from Bacterial Fermentation of Undigested Carbohydrate in Irritable Bowel Syndrome, *Am. J. Gastroenterol.* 84 (1989) 375–378. doi:10.1111/j.1572-0241.1989.tb02530.x.
- [16] M. Pimentel, Breath Testing for Small Intestinal Bacterial Overgrowth: Should We Bother?, *Am. J. Gastroenterol.* 111 (2016) 307–308. doi:10.1038/ajg.2016.30.
- [17] R. Khoshini, S.-C. Dai, S. Lezcano, M. Pimentel, A Systematic Review of Diagnostic Tests for Small

- Intestinal Bacterial Overgrowth, *Dig. Dis. Sci.* 53 (2008) 1443–1454. doi:10.1007/s10620-007-0065-1.
- [18] H.-T. Wang, T.J. Anderson, B.S. Kang, F. Ren, C. Li, Z.-N. Low, J. Lin, B.P. Gila, S.J. Pearton, A. Osinsky, A. Dabiran, Stable hydrogen sensors from AlGaIn/GaN heterostructure diodes with TiB₂-based Ohmic contacts, *Appl. Phys. Lett.* 90 (2007) 252109. doi:10.1063/1.2751107.
- [19] H. Gu, Z. Wang, Y. Hu, Hydrogen Gas Sensors Based on Semiconductor Oxide Nanostructures, *Sensors*. 12 (2012) 5517–5550. doi:10.3390/s120505517.
- [20] O. Lupan, V. Postica, T. Pauporté, B. Viana, M.-I. Terasa, R. Adelung, Room temperature gas nanosensors based on individual and multiple networked Au-modified ZnO nanowires, *Sensors Actuators B Chem.* 299 (2019) 126977. doi:10.1016/j.snb.2019.126977.
- [21] O. Lupan, V. V Ursaki, G. Chai, L. Chow, G.A. Emelchenko, I.M. Tiginyanu, A.N. Gruzintsev, A.N. Redkin, Selective hydrogen gas nanosensor using individual ZnO nanowire with fast response at room temperature, *Sensors Actuators B Chem.* 144 (2010) 56–66. doi:https://doi.org/10.1016/j.snb.2009.10.038.
- [22] Q. QI, T. ZHANG, X. ZHENG, H. FAN, L. LIU, R. WANG, Y. ZENG, Electrical response of Sm₂O₃-doped SnO₂ to C₂H₂ and effect of humidity interference, *Sensors Actuators B Chem.* 134 (2008) 36–42. doi:10.1016/j.snb.2008.04.011.
- [23] J. Gong, Q. Chen, M.-R. Lian, N.-C. Liu, R.G. Stevenson, F. Adami, Micromachined nanocrystalline silver doped SnO₂ H₂S sensor, *Sensors Actuators B Chem.* 114 (2006) 32–39. doi:10.1016/j.snb.2005.04.035.
- [24] O. Lupan, V. Postica, N. Wolff, J. Su, F. Labat, I. Ciofini, H. Cavers, R. Adelung, O. Polonskyi, F. Faupel, L. Kienle, B. Viana, T. Pauporté, Low-Temperature Solution Synthesis of Au-Modified ZnO Nanowires for Highly Efficient Hydrogen Nanosensors, *ACS Appl. Mater. Interfaces.* 11 (2019) 32115–32126. doi:10.1021/acsami.9b08598.
- [25] S. Wicker, M. Guiltat, U. Weimar, A. Hémerlyck, N. Barsan, Ambient Humidity Influence on CO Detection with SnO₂ Gas Sensing Materials. A Combined DRIFTS/DFT Investigation, *J. Phys. Chem. C.* 121 (2017) 25064–25073. doi:10.1021/acs.jpcc.7b06253.
- [26] C. Wang, L. Yin, L. Zhang, D. Xiang, R. Gao, Metal Oxide Gas Sensors: Sensitivity and Influencing Factors, *Sensors*. 10 (2010) 2088–2106. doi:10.3390/s100302088.
- [27] S.Y. Park, Y.H. Kim, S.Y. Lee, W. Sohn, J.E. Lee, D.H. Kim, Y.-S. Shim, K.C. Kwon, K.S. Choi, H.J. Yoo, J.M. Suh, M. Ko, J.-H. Lee, M.J. Lee, S.Y. Kim, M.H. Lee, H.W. Jang, Highly selective and sensitive chemoresistive humidity sensors based on rGO/MoS₂ van der Waals composites, *J. Mater. Chem. A.* 6 (2018) 5016–5024. doi:10.1039/C7TA11375G.
- [28] K.J. Choi, H.W. Jang, One-Dimensional Oxide Nanostructures as Gas-Sensing Materials: Review and Issues, *Sensors*. 10 (2010) 4083–4099. doi:10.3390/s100404083.
- [29] A. Gurlo, Nanosensors: towards morphological control of gas sensing activity. SnO₂, In₂O₃, ZnO and WO₃ case studies, *Nanoscale.* 3 (2011) 154–165. doi:10.1039/C0NR00560F.
- [30] O. Lupan, V. Cretu, V. Postica, N. Ababii, O. Polonskyi, V. Kaidas, F. Schütt, Y.K. Mishra, E. Monaico, I. Tiginyanu, V. Sontea, T. Strunskus, F. Faupel, R. Adelung, Enhanced ethanol vapour sensing performances of copper oxide nanocrystals with mixed phases, *Sensors Actuators B Chem.* 224 (2016) 434–448. doi:10.1016/j.snb.2015.10.042.
- [31] W.F. Stickle, P.E. Sobol, K.D. Bomben, *Handbook of X-ray photoelectron spectroscopy*, Eden Prairie, MN Perkin Elmer. (1992).

- [32] O. Lupan, N. Ababii, A.K. Mishra, O. Gronenberg, A. Vahl, U. Schürmann, V. Duppel, H. Krüger, L. Chow, L. Kienle, F. Faupel, R. Adelung, N.H. de Leeuw, S. Hansen, Single CuO/Cu₂O/Cu Microwire Covered by a Nanowire Network as a Gas Sensor for the Detection of Battery Hazards, *ACS Appl. Mater. Interfaces*. 12 (2020) 42248–42263. doi:10.1021/acsami.0c09879.
- [33] N. Helwig, M. Schüler, C. Bur, A. Schütze, T. Sauerwald, Gas mixing apparatus for automated gas sensor characterization, *Meas. Sci. Technol.* 25 (2014) 055903. doi:10.1088/0957-0233/25/5/055903.
- [34] S. Luo, Y. Shen, Z. Wu, M. Cao, F. Gu, L. Wang, Enhanced ethanol sensing performance of mesoporous Sn-doped ZnO, *Mater. Sci. Semicond. Process.* 41 (2016) 535–543. doi:10.1016/j.mssp.2015.10.001.
- [35] V. Postica, J. Gröttrup, R. Adelung, O. Lupan, A.K. Mishra, N.H. de Leeuw, N. Ababii, J.F.C. Carreira, J. Rodrigues, N. Ben Sedrine, M.R. Correia, T. Monteiro, V. Sontea, Y.K. Mishra, Multifunctional Materials: A Case Study of the Effects of Metal Doping on ZnO Tetrapods with Bismuth and Tin Oxides, *Adv. Funct. Mater.* 27 (2017) 1604676. doi:10.1002/adfm.201604676.
- [36] P.E. Blöchl, Projector augmented-wave method, *Phys. Rev. B*. 50 (1994) 17953–17979. doi:10.1103/PhysRevB.50.17953.
- [37] G. Kresse, D. Joubert, From ultrasoft pseudopotentials to the projector augmented-wave method, *Phys. Rev. B*. 59 (1999) 1758–1775. doi:10.1103/PhysRevB.59.1758.
- [38] G. Kresse, J. Hafner, Ab initio molecular dynamics for liquid metals, *Phys. Rev. B*. 47 (1993) 558–561. doi:10.1103/PhysRevB.47.558.
- [39] G. Kresse, J. Hafner, Ab initio molecular-dynamics simulation of the liquid-metal–amorphous-semiconductor transition in germanium, *Phys. Rev. B*. 49 (1994) 14251–14269. doi:10.1103/PhysRevB.49.14251.
- [40] G. Kresse, J. Furthmüller, Efficiency of ab-initio total energy calculations for metals and semiconductors using a plane-wave basis set, *Comput. Mater. Sci.* 6 (1996) 15–50. doi:10.1016/0927-0256(96)00008-0.
- [41] G. Kresse, J. Furthmüller, Efficient iterative schemes for ab initio total-energy calculations using a plane-wave basis set, *Phys. Rev. B*. 54 (1996) 11169–11186. doi:10.1103/PhysRevB.54.11169.
- [42] J.P. Perdew, K. Burke, M. Ernzerhof, Generalized Gradient Approximation Made Simple, *Phys. Rev. Lett.* 77 (1996) 3865–3868. doi:10.1103/PhysRevLett.77.3865.
- [43] S.L. Dudarev, G.A. Botton, S.Y. Savrasov, C.J. Humphreys, A.P. Sutton, Electron-energy-loss spectra and the structural stability of nickel oxide: An LSDA+U study, *Phys. Rev. B*. 57 (1998) 1505–1509. doi:10.1103/PhysRevB.57.1505.
- [44] A.K. Mishra, A. Roldan, N.H. de Leeuw, CuO Surfaces and CO₂ Activation: A Dispersion-Corrected DFT+ U Study, *J. Phys. Chem. C*. 120 (2016) 2198–2214. doi:10.1021/acs.jpcc.5b10431.
- [45] A.K. Mishra, A. Roldan, N.H. de Leeuw, A density functional theory study of the adsorption behaviour of CO₂ on Cu₂O surfaces, *J. Chem. Phys.* 145 (2016) 044709. doi:10.1063/1.4958804.
- [46] H.J. Monkhorst, J.D. Pack, Special points for Brillouin-zone integrations, *Phys. Rev. B*. 13 (1976) 5188–5192. doi:10.1103/PhysRevB.13.5188.
- [47] S. Grimme, Semiempirical GGA-type density functional constructed with a long-range dispersion correction, *J. Comput. Chem.* 27 (2006) 1787–1799. doi:10.1002/jcc.20495.

- [48] G. Henkelman, A. Arnaldsson, H. Jónsson, A fast and robust algorithm for Bader decomposition of charge density, *Comput. Mater. Sci.* 36 (2006) 354–360. doi:10.1016/j.commatsci.2005.04.010.
- [49] R.F.W. Bader, *Atoms in molecules : a quantum theory*, Oxford University Press: London, 1994. <https://global.oup.com/academic/product/atoms-in-molecules-9780198558651#.XsEQe5nJ4Lg.mendeley> (accessed May 17, 2020).
- [50] E. Ghanti, R. Nagarajan, Synthesis of $\text{CuAl}_2(\text{acac})_4(\text{O}^i\text{Pr})_4$, its hydrolysis and formation of bulk CuAl_2O_4 from the hydrolyzed gels; a case study of molecules to materials, *Dalt. Trans.* 39 (2010) 6056. doi:10.1039/b926579a.
- [51] N. Tomar, E. Ghanti, A.K. Bhagi, R. Nagarajan, Studies on the hydrolysis of $\{\text{Cu}[\text{Al}(\text{OPr}^i)_4]_2\}$, a single source precursor for CuAl_2O_4 spinel, *J. Non. Cryst. Solids.* 355 (2009) 2657–2662. doi:10.1016/j.jnoncrsol.2009.08.026.
- [52] M. Salavati-Niasari, F. Davar, M. Farhadi, Synthesis and characterization of spinel-type CuAl_2O_4 nanocrystalline by modified sol–gel method, *J. Sol-Gel Sci. Technol.* 51 (2009) 48–52. doi:10.1007/s10971-009-1940-3.
- [53] S. Åsbrink, L.J. Norrby, A refinement of the crystal structure of copper(II) oxide with a discussion of some exceptional e.s.d.'s, *Acta Crystallogr. Sect. B Struct. Crystallogr. Cryst. Chem.* 26 (1970) 8–15. doi:10.1107/S0567740870001838.
- [54] I.M. Tiginyanu, O. Lupan, V.V. Ursaki, L. Chow, M. Enachi, Nanostructures of Metal Oxides, in: P. Bhattacharya, R. Fornari, H. Kamimura (Eds.), *Compr. Semicond. Sci. Technol.*, Elsevier, Amsterdam, 2011: pp. 396–479. doi:10.1016/B978-0-44-453153-7.00105-X.
- [55] L. Debbichi, M.C. Marco de Lucas, J.F. Pierson, P. Krüger, Vibrational Properties of CuO and Cu_4O_3 from First-Principles Calculations, and Raman and Infrared Spectroscopy, *J. Phys. Chem. C.* 116 (2012) 10232–10237. doi:10.1021/jp303096m.
- [56] D. Wu, Q. Zhang, M. Tao, LSDA+U study of cupric oxide: Electronic structure and native point defects, *Phys. Rev. B.* 73 (2006) 235206–235212. doi:10.1103/PhysRevB.73.235206.
- [57] J.D. Hanawalt, H.W. Rinn, L.K. Frevel, *Chemical Analysis by X-Ray Diffraction*, *Ind. Eng. Chem. Anal. Ed.* 10 (1938) 457–512. doi:10.1021/ac50125a001.
- [58] G. Kliche, Z. V Popovic, Far-infrared spectroscopic investigations on CuO , *Phys. Rev. B.* 42 (1990) 10060–10066. doi:10.1103/PhysRevB.42.10060.
- [59] H. Shirai, Y. Morioka, I. Nakagawa, Infrared and Raman Spectra and Lattice Vibrations of Some Oxide Spinel, *J. Phys. Soc. Japan.* 51 (1982) 592–597. doi:10.1143/JPSJ.51.592.
- [60] M.A. Laguna-Bercero, M.L. Sanjuán, R.I. Merino, Raman spectroscopic study of cation disorder in poly- and single crystals of the nickel aluminate spinel, *J. Phys. Condens. Matter.* 19 (2007) 186217. doi:10.1088/0953-8984/19/18/186217.
- [61] N. Ababii, M. Hoppe, S. Shree, A. Vahl, M. Ulfa, T. Pauporté, B. Viana, V. Cretu, N. Magariu, V. Postica, V. Sontea, M.-I. Terasa, O. Polonskyi, F. Faupel, R. Adelung, O. Lupan, Effect of noble metal functionalization and film thickness on sensing properties of sprayed TiO_2 ultra-thin films, *Sensors Actuators A Phys.* 293 (2019) 242–258. doi:10.1016/j.sna.2019.04.017.
- [62] F. Guanghui, D. Jiafeng, P. Donghui, H. Ouli, The migration of alkali ions from glass substrates coated with sol-gel barrier films, *J. Non. Cryst. Solids.* 112 (1989) 454–457. doi:10.1016/0022-3093(89)90572-3.
- [63] A. Loubat, M. Bouttemy, S. Gaiaschi, D. Aureau, M. Frégnaux, D. Mercier, J. Vigneron, P. Chapon,

- A. Etcheberry, Chemical engineering of Cu(In,Ga)Se₂ surfaces: An absolute deoxidation studied by X-ray photoelectron spectroscopy and Auger electron spectroscopy signatures, *Thin Solid Films*. 633 (2017) 87–91. doi:10.1016/j.tsf.2016.10.013.
- [64] A. V Naumkin, A. Kraust-Vass, S.W. Gaarenstroom, C.J. Powell, NIST X-ray Photoelectron Spectroscopy Database, National Institute of Standards and Technology, NIST Stand. Ref. Database Number 20. (2000). doi:10.18434/T4T88K.
- [65] N. Pauly, S. Tougaard, F. Yubero, Determination of the Cu 2p primary excitation spectra for Cu, Cu₂O and CuO, *Surf. Sci.* 620 (2014) 17–22. doi:10.1016/j.susc.2013.10.009.
- [66] A. Vahl, J. Dittmann, J. Jetter, S. Veziroglu, S. Shree, N. Ababii, O. Lupan, O.C. Aktas, T. Strunskus, E. Quandt, R. Adelung, S.K. Sharma, F. Faupel, The impact of O₂/Ar ratio on morphology and functional properties in reactive sputtering of metal oxide thin films, *Nanotechnology*. 30 (2019) 235603. doi:10.1088/1361-6528/ab0837.
- [67] A.W. Golubkov, D. Fuchs, J. Wagner, H. Wiltse, C. Stangl, G. Fauler, G. Voitic, A. Thaler, V. Hacker, Thermal-runaway experiments on consumer Li-ion batteries with metal-oxide and olivine-type cathodes, *RSC Adv.* 4 (2014) 3633–3642. doi:10.1039/c3ra45748f.
- [68] M. Metzger, B. Strehle, S. Solchenbach, H.A. Gasteiger, Origin of H₂ Evolution in LIBs: H₂O Reduction vs. Electrolyte Oxidation, *J. Electrochem. Soc.* 163 (2016) A798–A809. doi:10.1149/2.1151605jes.
- [69] D. Ortiz, V. Steinmetz, D. Durand, S. Legand, V. Dauvois, P. Maître, S. Le Caër, Radiolysis as a solution for accelerated ageing studies of electrolytes in Lithium-ion batteries, *Nat. Commun.* 6 (2015) 6950. doi:10.1038/ncomms7950.
- [70] N.E. Galushkin, N.N. Yazvinskaya, D.N. Galushkin, Mechanism of Gases Generation during Lithium-Ion Batteries Cycling, *J. Electrochem. Soc.* 166 (2019) A897–A908. doi:10.1149/2.0041906jes.
- [71] V. Mateev, I. Marinova, Z. Kartunov, Gas Leakage Source Detection for Li-Ion Batteries by Distributed Sensor Array, *Sensors*. 19 (2019) 2900. doi:10.3390/s19132900.
- [72] M. Wenger, R. Waller, V.R.H. Lorentz, M. Marz, M. Herold, Investigation of gas sensing in large lithium-ion battery systems for early fault detection and safety improvement, in: *IECON 2014 - 40th Annu. Conf. IEEE Ind. Electron. Soc., IEEE, 2014*: pp. 5654–5659. doi:10.1109/IECON.2014.7049366.
- [73] O. Lupan, V. Postica, J. Gröttrup, A.K. Mishra, N.H. de Leeuw, J.F.C. Carreira, J. Rodrigues, N. Ben Sedrine, M.R. Correia, T. Monteiro, V. Cretu, I. Tiginyanu, D. Smazna, Y.K. Mishra, R. Adelung, Hybridization of Zinc Oxide Tetrapods for Selective Gas Sensing Applications, *ACS Appl. Mater. Interfaces*. 9 (2017) 4084–4099. doi:10.1021/acsami.6b11337.
- [74] L. Siebert, N. Wolff, N. Ababii, M.-I. Terasa, O. Lupan, A. Vahl, V. Duppel, H. Qiu, M. Tienken, M. Mirabelli, V. Sontea, F. Faupel, L. Kienle, R. Adelung, Facile fabrication of semiconducting oxide nanostructures by direct ink writing of readily available metal microparticles and their application as low power acetone gas sensors, *Nano Energy*. 70 (2020) 104420. doi:10.1016/j.nanoen.2019.104420.
- [75] L. Siebert, O. Lupan, M. Mirabelli, N. Ababii, M.-I. Terasa, S. Kaps, V. Cretu, A. Vahl, F. Faupel, R. Adelung, 3D-Printed Chemiresistive Sensor Array on Nanowire CuO/Cu₂O/Cu Heterojunction Nets, *ACS Appl. Mater. Interfaces*. 11 (2019) 25508–25515. doi:10.1021/acsami.9b04385.
- [76] M. Hoppe, N. Ababii, V. Postica, O. Lupan, O. Polonskyi, F. Schütt, S. Kaps, L.F. Sukhodub, V. Sontea, T. Strunskus, F. Faupel, R. Adelung, (CuO-Cu₂O)/ZnO:Al heterojunctions for volatile

- organic compound detection, *Sensors Actuators B Chem.* 255 (2018) 1362–1375. doi:10.1016/j.snb.2017.08.135.
- [77] J. Gröttrup, V. Postica, N. Ababii, O. Lupan, C. Zamponi, D. Meyners, Y.K. Mishra, V. Sontea, I. Tiginyanu, R. Adelung, Size-dependent UV and gas sensing response of individual Fe₂O₃-ZnO:Fe micro- and nanowire based devices, *J. Alloys Compd.* 701 (2017) 920–925. doi:10.1016/j.jallcom.2016.12.346.
- [78] N. Barsan, U. Weimar, Conduction Model of Metal Oxide Gas Sensors, *J. Electroceramics.* 7 (2001) 143–167. doi:10.1023/A:1014405811371.
- [79] Y. Wang, K. Wu, As a Whole: Crystalline Zinc Aluminate Nanotube Array–Nanonet, *J. Am. Chem. Soc.* 127 (2005) 9686–9687. doi:10.1021/ja0505402.
- [80] M. Hoppe, O. Lupan, V. Postica, N. Wolff, V. Duppel, L. Kienle, I. Tiginyanu, R. Adelung, ZnAl₂O₄ - Functionalized Zinc Oxide Microstructures for Highly Selective Hydrogen Gas Sensing Applications, *Phys. Status Solidi.* 215 (2018) 1700772. doi:10.1002/pssa.201700772.
- [81] C.R. Michel, CO and CO₂ gas sensing properties of mesoporous CoAl₂O₄, *Sensors Actuators B Chem.* 147 (2010) 635–641. doi:10.1016/j.snb.2010.04.013.
- [82] D. Dhak, P. Pramanik, Particle Size Comparison of Soft-Chemically Prepared Transition Metal (Co, Ni, Cu, Zn) Aluminate Spinel, *J. Am. Ceram. Soc.* 89 (2006) 1014–1021. doi:10.1111/j.1551-2916.2005.00769.x.
- [83] O. Lupan, V. Cretu, V. Postica, O. Polonskyi, N. Ababii, F. Schütt, V. Kaidas, F. Faupel, R. Adelung, Non-planar nanoscale p–p heterojunctions formation in Zn_xCu_{1-x}O_y nanocrystals by mixed phases for enhanced sensors, *Sensors Actuators B Chem.* 230 (2016) 832–843. doi:10.1016/j.snb.2016.02.089.
- [84] X. Zhao, L. Wang, X. Xu, X. Lei, S. Xu, F. Zhang, Fabrication and photocatalytic properties of novel ZnO/ZnAl₂O₄ nanocomposite with ZnAl₂O₄ dispersed inside ZnO network, *AIChE J.* 58 (2012) 573–582. doi:10.1002/aic.12597.
- [85] H.-J. Kim, H.-M. Jeong, T.-H. Kim, J.-H. Chung, Y.C. Kang, J.-H. Lee, Enhanced Ethanol Sensing Characteristics of In₂O₃ -Decorated NiO Hollow Nanostructures via Modulation of Hole Accumulation Layers, *ACS Appl. Mater. Interfaces.* 6 (2014) 18197–18204. doi:10.1021/am5051923.
- [86] H.-R. Kim, K.-I. Choi, K.-M. Kim, I.-D. Kim, G. Cao, J.-H. Lee, Ultra-fast responding and recovering C₂H₅OH sensors using SnO₂ hollow spheres prepared and activated by Ni templates, *Chem. Commun.* 46 (2010) 5061. doi:10.1039/c0cc00213e.
- [87] O. Lupan, L. Chow, G. Chai, A single ZnO tetrapod-based sensor, *Sensors Actuators B Chem.* 141 (2009) 511–517. doi:10.1016/j.snb.2009.07.011.
- [88] O. Lupan, L. Chow, T. Pauporté, L.K. Ono, B. Roldan Cuenya, G. Chai, Highly sensitive and selective hydrogen single-nanowire nanosensor, *Sensors Actuators B Chem.* 173 (2012) 772–780. doi:10.1016/j.snb.2012.07.111.
- [89] Y.-H. Choi, D.-H. Kim, S.-H. Hong, K.S. Hong, H₂ and C₂H₅OH sensing characteristics of mesoporous p-type CuO films prepared via a novel precursor-based ink solution route, *Sensors Actuators B Chem.* 178 (2013) 395–403. doi:10.1016/j.snb.2012.12.096.
- [90] M. Bersani, K. Gupta, A.K. Mishra, R. Lanza, S.F.R. Taylor, H.-U. Islam, N. Hollingsworth, C. Hardacre, N.H. de Leeuw, J.A. Darr, Combined EXAFS, XRD, DRIFTS, and DFT Study of Nano Copper-Based Catalysts for CO₂ Hydrogenation, *ACS Catal.* 6 (2016) 5823–5833.

doi:10.1021/acscatal.6b01529.

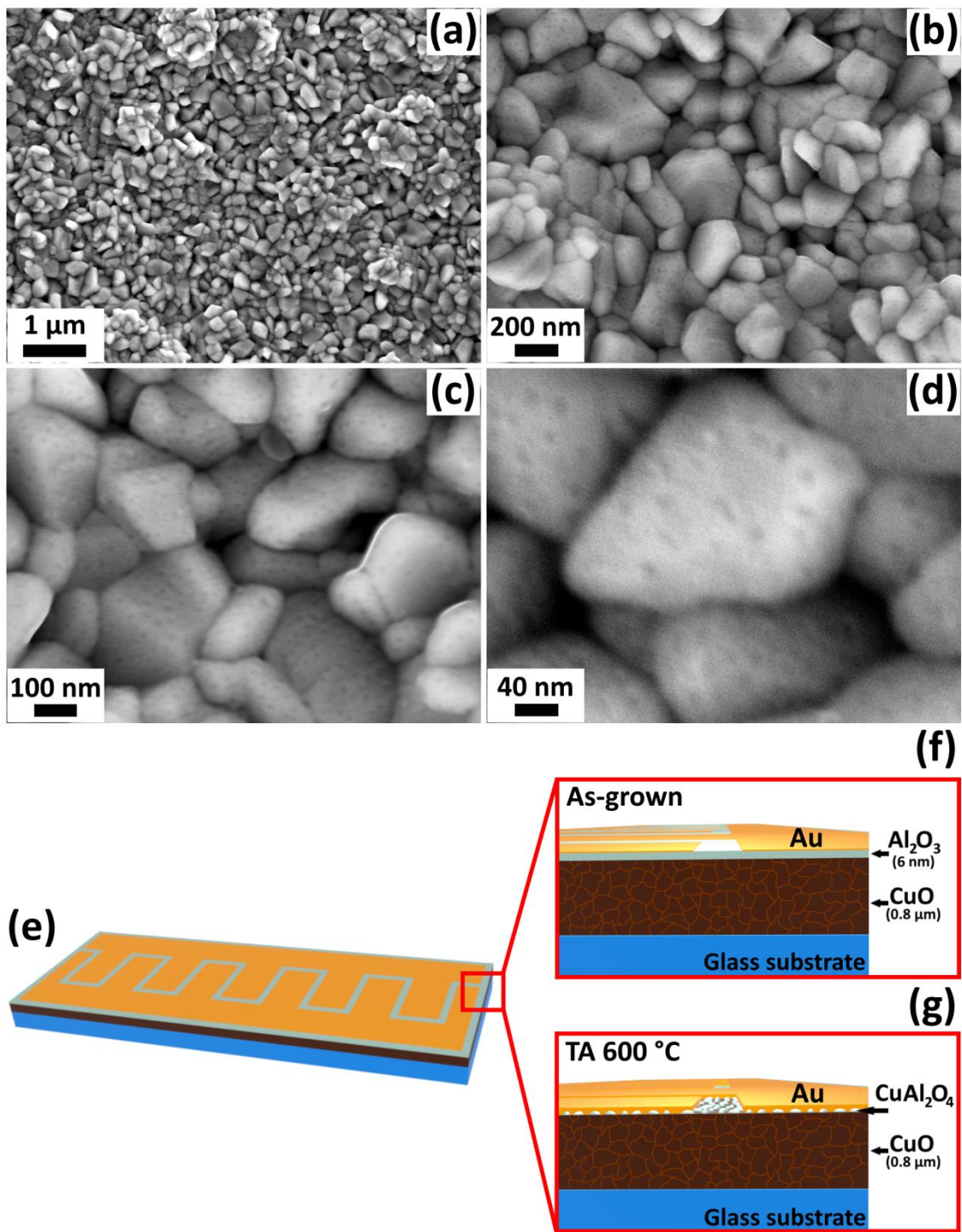


Figure 1. SEM images of 6 nm- $\text{Al}_2\text{O}_3/\text{CuO}$ heterostructures with thermal annealing at 600 °C for 30 min at various enlargement: (a) 1 μm ; (b) 200 nm; (c) 100 nm; and (d) 40 nm. (e) The schematic drawing of the detector made on the nano- $\text{Al}_2\text{O}_3/\text{CuO}$ heterostructure: (f) as-grown; and (g) TA 600 °C.

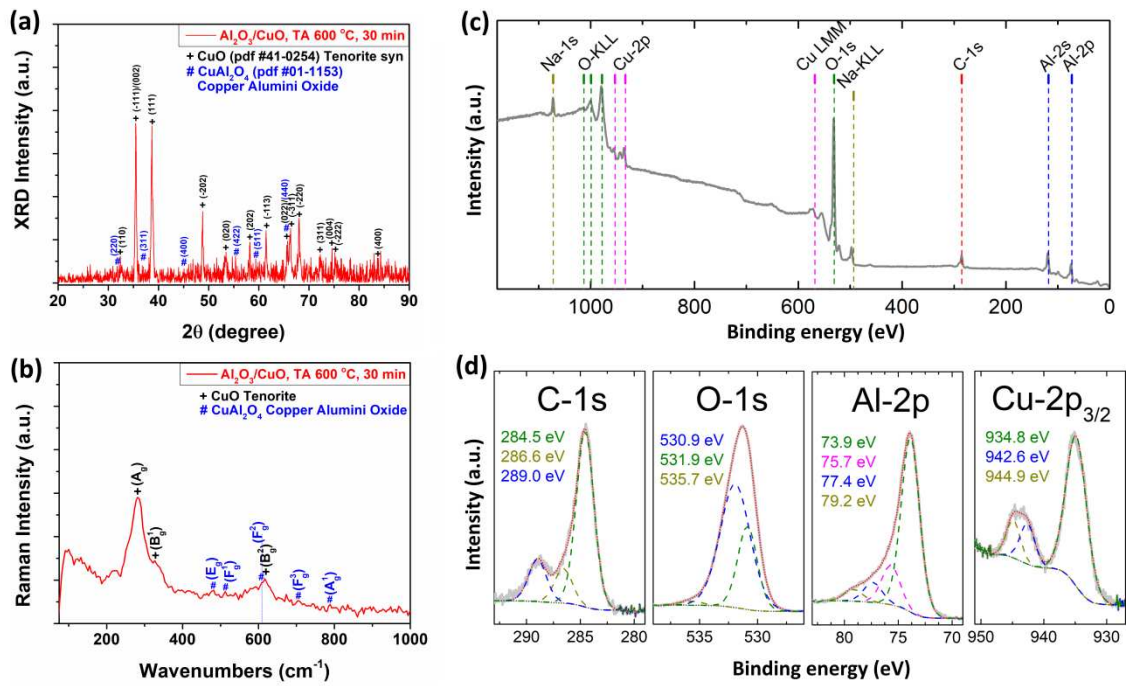


Figure 2. (a) XRD patterns; (b) room temperature Raman spectrum; (c) XPS analysis of 6 nm- $\text{Al}_2\text{O}_3/\text{CuO}$ heterostructures with thermal treated at 600 °C for 30 min indicates the presence of Na, Cu, O, Al and C. (d) The positions for peaks are shown by dashed lines in the survey spectrum. In the highresolution spectra, the C1s, O1s, Al2p and Cu2p lines are fitted and dashed lines show the peak positions of the respective components.

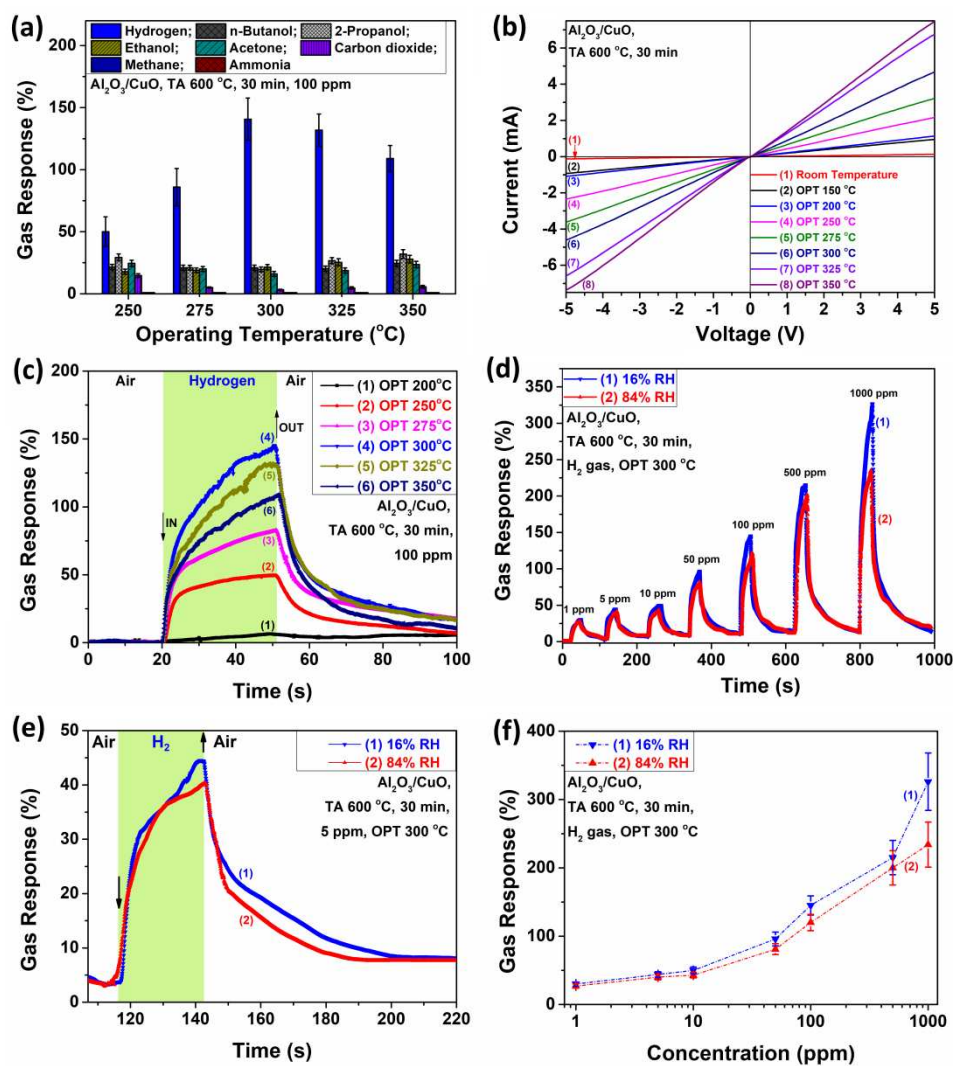


Figure 3. (a) Gas response to various gases (100 ppm) and work temperatures of 6 nm-Al₂O₃/CuO heterostructures with thermal treated at 600 °C for 30 min. (b) I/V-characteristics for Al₂O₃/CuO heterostructures treatment treated at 600 °C for 30 min at multiple work temperatures. (c) Dynamic response to 100 ppm of hydrogen gas for 6 nm-Al₂O₃/CuO heterostructures treatment treated at 600 °C for 30 min at multiple work temperatures. (d) Dynamic response to multiple concentrations of hydrogen (1, 5, 10, 50, 100, 500 and 1000 ppm) and work temperature of 300 °C of 6 nm-Al₂O₃/CuO heterostructures treatment annealing at 600 °C for 30 min for low and high relative humidity. (e) Dynamic response to 5 ppm of hydrogen gas for 6 nm-Al₂O₃/CuO heterostructures treatment annealing at 600 °C for 30 min at OPT 300 °C. (f) Response to different concentrations of hydrogen gas at work temperature of 300 °C for low and high relative humidity.

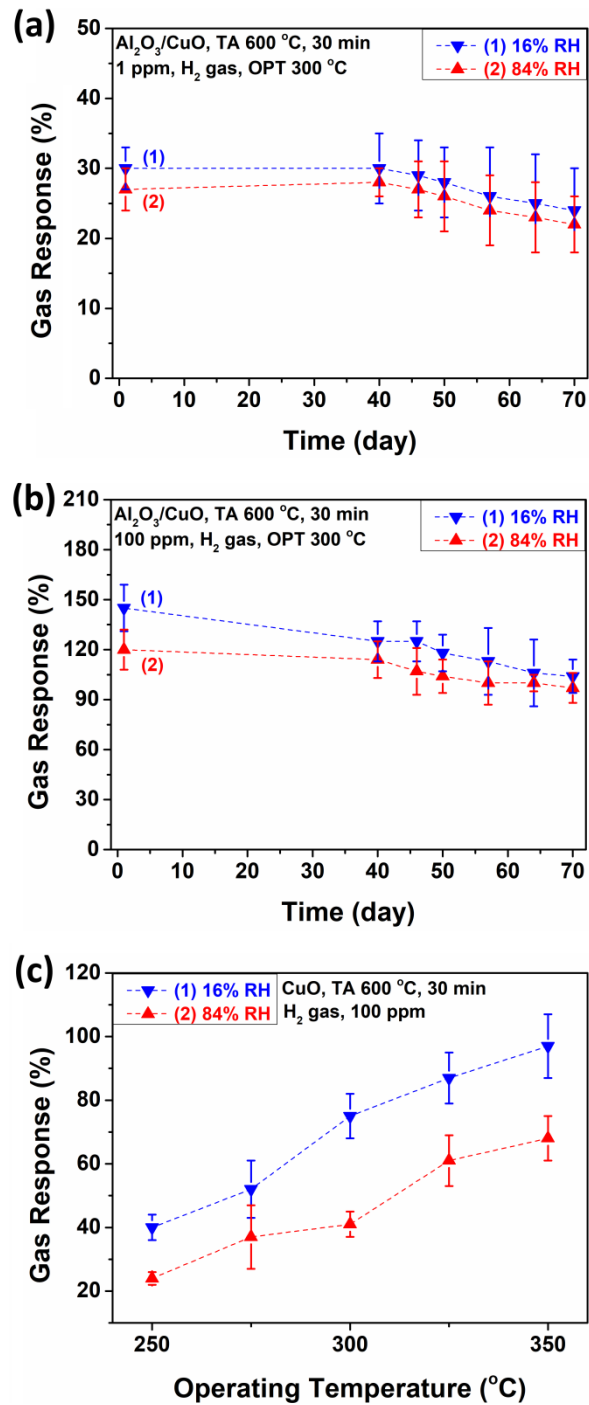


Figure 4. The long-term stability of 6 nm- $\text{Al}_2\text{O}_3/\text{CuO}$ heterostructures for low and high relative humidity at work temperature of 300 °C and the response to H_2 gas with concentrations of: (a) 1 ppm; and (b) 100 ppm. (c) Response to H_2 gas versus operating temperatures for low and high relative humidity of CuO nanostructures.

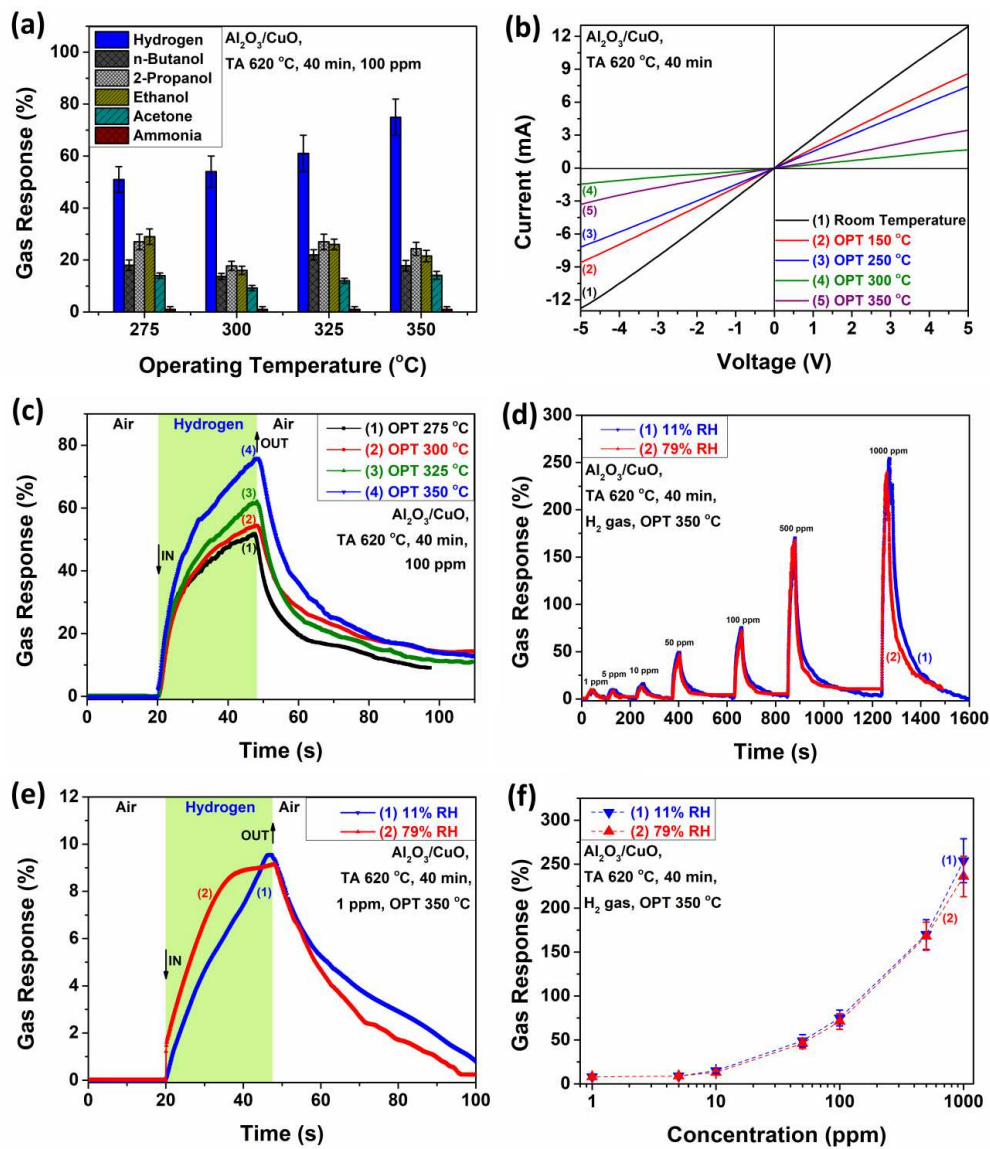


Figure 5. (a) Gas response to various gases (100 ppm) and work temperatures of 15 nm- $\text{Al}_2\text{O}_3/\text{CuO}$ heterostructures with thermal annealing at 620 °C for 40 min. (b) I/V-characteristics for 15 nm- $\text{Al}_2\text{O}_3/\text{CuO}$ heterostructures with thermal annealing at 620 °C for 40 min at different operating temperatures. (c) Dynamic response to 100 ppm of hydrogen gas for 15 nm- $\text{Al}_2\text{O}_3/\text{CuO}$ heterostructures with thermal annealing at 620 °C for 40 min at different operating temperatures. (d) Dynamic response to different concentrations of hydrogen (1, 5, 10, 50, 100, 500 and 1000 ppm) and work temperature of 350 °C of 15 nm- $\text{Al}_2\text{O}_3/\text{CuO}$ heterostructures with thermal annealing at 620 °C for 40 min for low and high relative humidity. (e) Dynamic response to 1 ppm of hydrogen gas for 15 nm- $\text{Al}_2\text{O}_3/\text{CuO}$ heterostructures with thermal annealing at 620 °C for 40

min at OPT 300 °C. (f) Response to multiple concentrations of hydrogen gas at work temperature of 350 °C for low and high relative humidity.

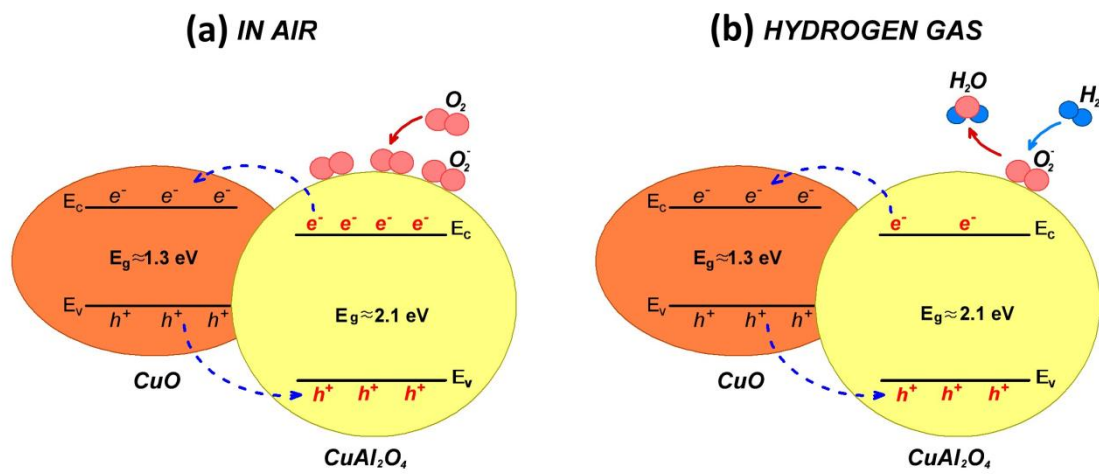


Figure 6. Schematic illustration of the H₂ detecting mechanism for CuAl₂O₄/CuO heterostructure: (a) under ambient atmosphere; and (b) under hydrogen gas.

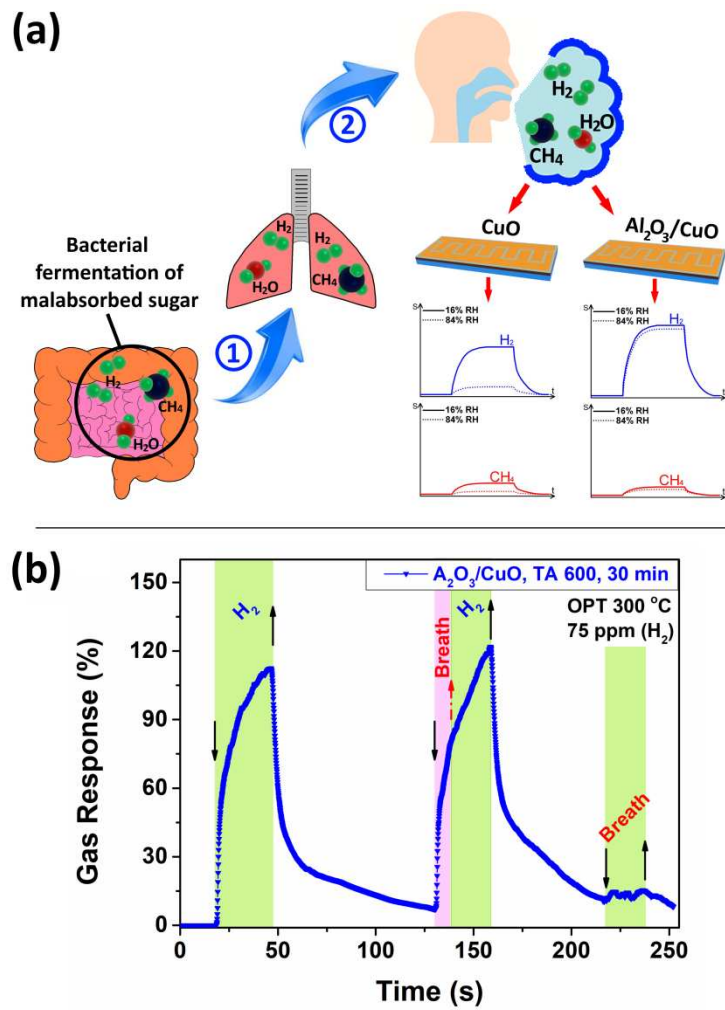


Figure 7. (a) Schematic of principle of hydrogen and/or methane breath test; (b) the influence of breath from a healthy person on the hydrogen response.

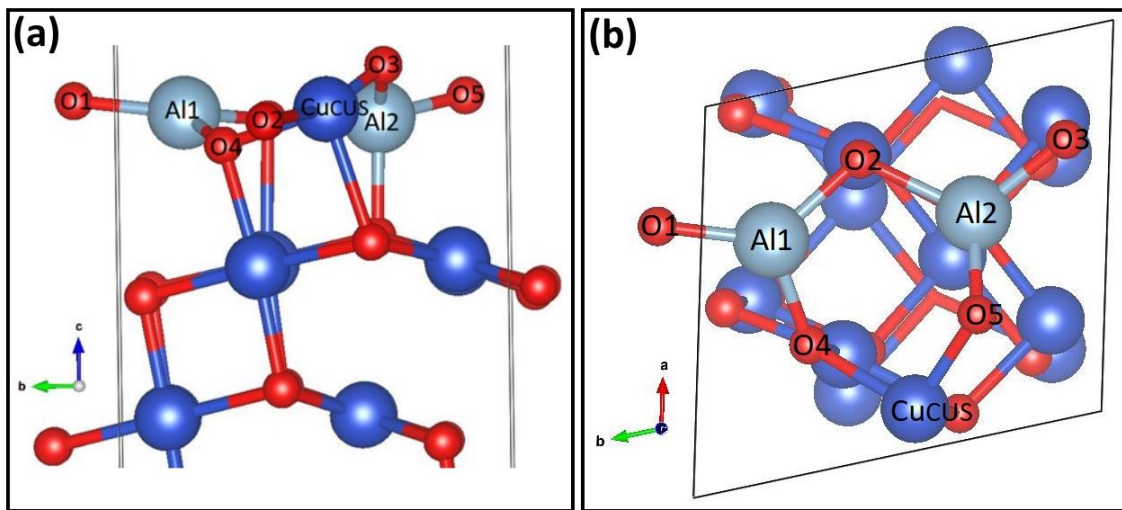


Figure 8. Side (a) and top view (b) of the relaxed structure of the $\text{Al}_2\text{O}_3\text{-CuO}$ (111) surface, where O = red, Al = light blue, and Cu = dark blue.

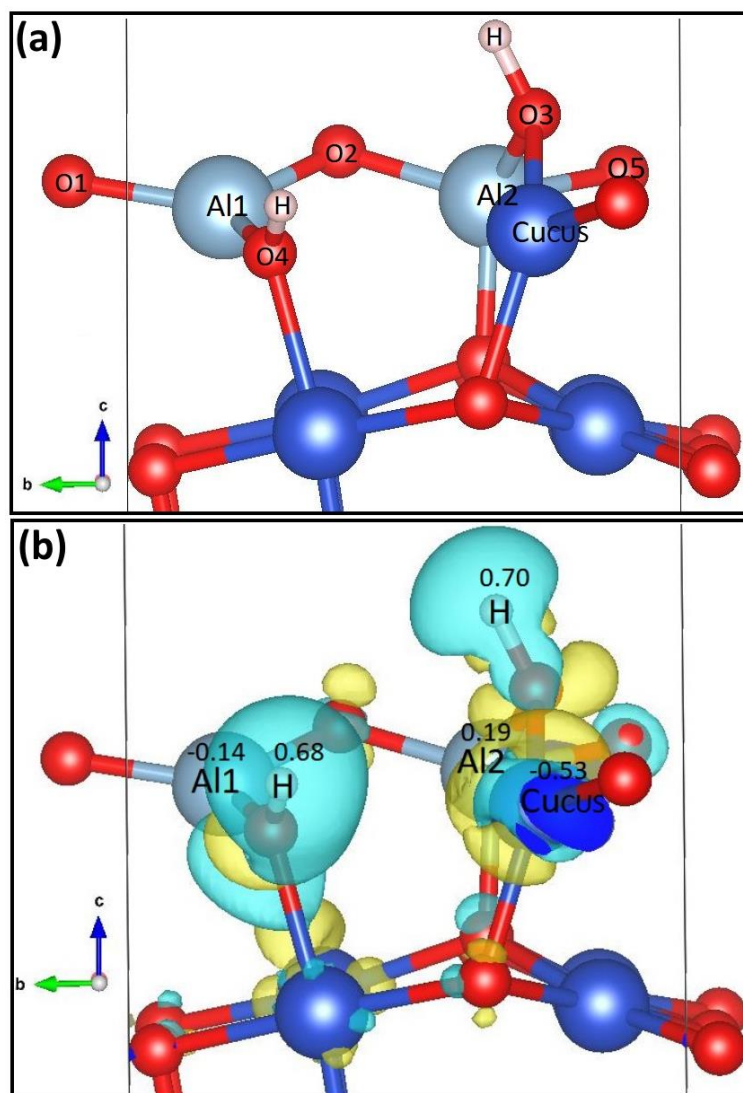


Figure 9. (a) Interaction of Hydrogen molecule with Al₂O₃-CuO (111) surface. Hydrogen atoms are shown in salmon pink, whereas the colour scheme of the other atoms is the same as in Fig. 8; (b) Charge density difference plot of H₂ molecule interaction on the Al₂O₃-CuO (111) surface, where positive and negative charge densities in (e/Bohr³) are indicated by yellow and blue colours. Different numbers indicate bader charges on atoms. Colour scheme for the atoms is the same as in (a).

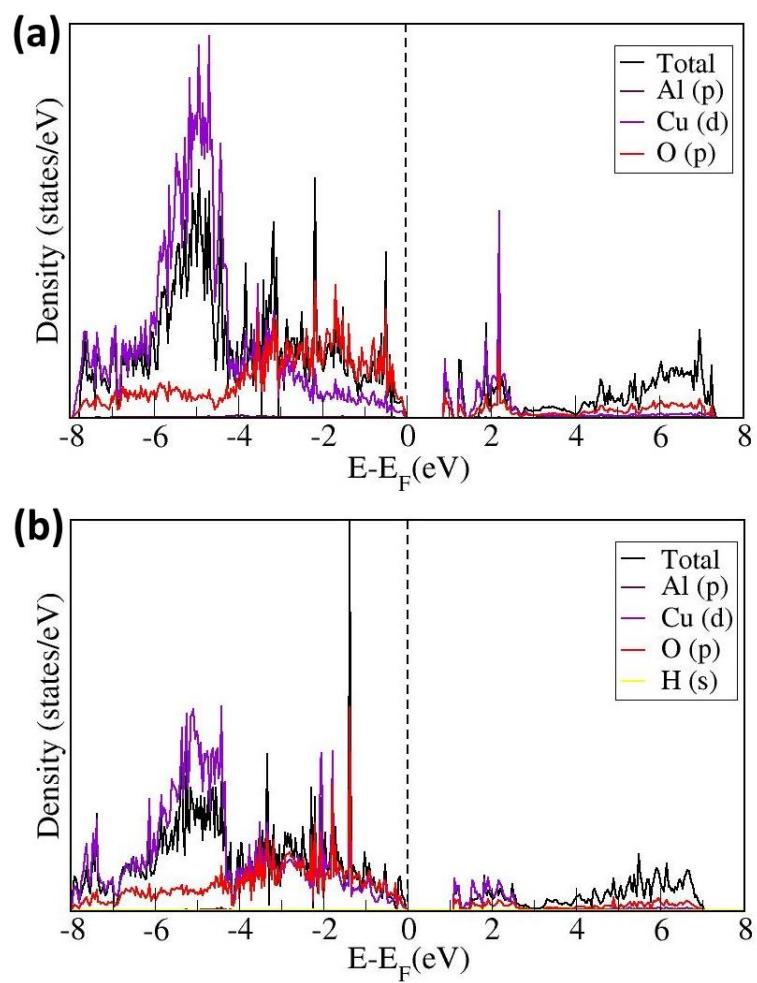


Figure 10. Density of states of (a) the $\text{Al}_2\text{O}_3\text{-CuO}(111)$ surface, and (b) the system of the Hydrogen molecule adsorbed on the $\text{Al}_2\text{O}_3\text{-CuO}(111)$ surface.

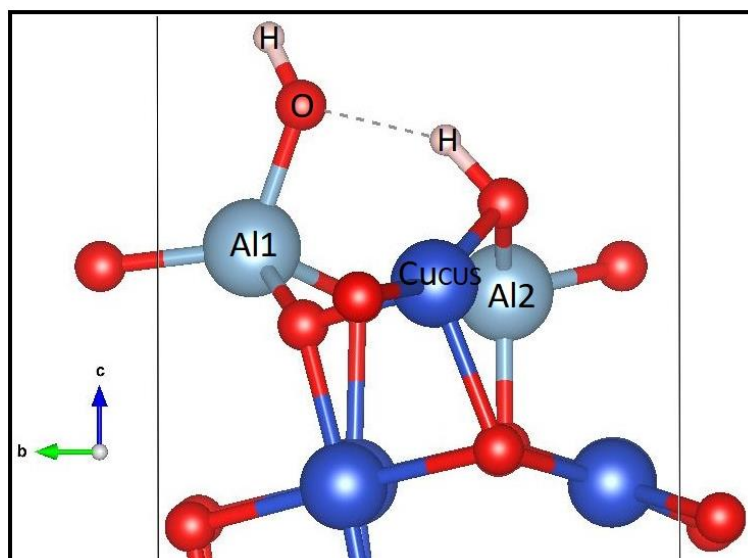


Figure 11. H₂O molecule interaction with Al₂O₃-CuO (111) surface. Hydrogen atoms are represented by salmon pink colour, while other atoms colour scheme is same as in Fig.8.